

Materials Characterization for Microwave Atom Chip Development

A thesis submitted in partial fulfillment of the requirement
for the degree of Bachelor of Science with Honors in
Physics from the College of William and Mary in Virginia,

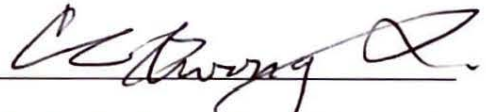
by

Jordan M. Shields

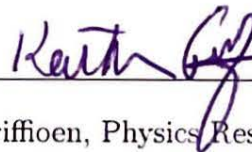
Accepted for ^{Honors} Honors



Prof. Seth. A. Aubin, Advisor



Prof. Chi-Kwong Li, Mathematics



Prof. Keith Griffioen, Physics Research Coordinator

Williamsburg, Virginia

May 3, 2023

Contents

Acknowledgements	iii
Abstract	i
List of Figures	v
List of Tables	vi
1 Introduction	1
1.1 Motivation	1
1.2 Structure of Thesis	2
2 Theory	4
2.1 Atom trap theory	4
2.1.1 AC Zeeman Effect	5
2.1.2 Dressed Atom Theory	6
2.2 Atom Interferometry	9
2.3 Cavity Theory	10
2.4 Parallel-plate Capacitor Theory	13
3 Measuring the Dielectric Constant and Loss Tangent of Aluminum Nitride	14
3.1 Parallel-plate Capacitor Approach	14
3.2 Resonator Approach	19

3.2.1	Sonnet Simulations	19
3.2.2	Ansys HFSS Simulations	21
3.2.3	Experimental Results	23
3.2.4	Extracting the Dielectric Constant	26
3.2.5	Extracting the Loss Tangent	31
4	Power Testing of Current Co-planar Waveguides and Microstrips	36
4.1	Expermental Setup	36
4.1.1	Challenges in Adhering Wires to CPWs	37
4.2	Results	40
5	Characterizing Quality of AlN and Alumina Samples	43
5.1	Surface Roughness Measurements	44
5.2	Characterizing Quality of the Cuts	46
5.2.1	15 mm Cu-AlN-Cu Samples	47
5.2.2	22 mm Cu-AlN-Cu Samples	48
5.2.3	15 mm Cu-Alumina-Cu Samples	50
5.2.4	22 mm Cu-Alumina-Cu Samples	51
6	Conclusion and Future Research	54
	Appendices	57
	A Python program for creating plots from Sonnet, HFSS, or VNA data	58
	B Python program for finding resonance spacing and percent difference	60
	C Python program for plotting power testing data from an oscilloscope	63
	D Creating gap resonators in Sonnet	65
	Bibliography	66

Acknowledgements

First and foremost, I would like to thank Dr. Seth Aubin for supporting my research and undergraduate career as well as the rest of the Aubin lab for their help and continued support throughout my project. Namely, I would like to thank William Miyahira for his advice and showing me how to use various equipment and simulation software. I would also like to thank the William and Mary Applied Research Center Core Labs - in particular, Doug Beringer and Olga Trofimova, for training me on and allowing me to use the equipment there. Additionally, I would like to thank Dr. Keith Griffioen and Dr. Chi-Kwong Li for being on my thesis committee and providing feedback and support of my work. Finally, I would like to thank the William and Mary physics department as a whole for their encouragement and guidance as I found my footing as a future physicist and researcher.

Public Abstract

The Aubin lab at William and Mary seeks to develop a chip that can trap and move atoms using microwaves. The atoms to be used with this chip have an inherent property known as “spin”, which can be “up” or “down” for each atom. Using a phenomenon known as the AC Zeeman effect, the chip can trap atoms of a specific spin and repel atoms of the other spin. This is useful for applications that rely on spatially separating atoms of different spin, such as an atom-based interferometer, which is a precision measurement tool.

The chip is made of a backing material (substrate) with lines of copper on top of it. This thesis describes research in measuring properties of the substrate; the measurement techniques were tested on a substrate with well-known properties, Rogers RO4350B, in order to provide proof-of-concept so they can then be applied to the substrate to be used in the chip, aluminum nitride (AlN). Namely, the measurement of the following is described: (1) the dielectric constant, a measure of the material’s ability to store electrical energy, (2) the maximum power (current) that can be applied to the chip, and (3) the roughness and quality of samples to be used in creating the chip. The next steps of this research are to measure the loss tangent of RO4350B, a measure of a material’s inherent dissipation of electromagnetic energy, then develop a way to effectively insert microwaves onto a chip made of AlN and measure the dielectric constant and loss tangent of AlN. Finally, using the results of this research, fabrication and testing of the chip can begin.

Physics Abstract

This thesis describes research to characterize materials to be implemented on a microwave atom trap chip, which will be able to trap and spatially manipulate atoms using the spin-specific microwave AC Zeeman effect. Potential applications of this research include atom-based interferometry and quantum computing.

Namely, this thesis describes the characterization of the following: (1) the dielectric constant of a well-characterized substrate, Rogers RO4350B, in order to provide proof-of-concept for a method that can be applied to the chip's substrate, aluminum nitride (AlN), (2) the maximum current that will be able to be applied to the chip, and (3) surface roughness and quality of cuts of samples to be utilized in creating the chip. In the broader context of the ultracold atom research in the Aubin Lab, characterizing these materials will be a major engineering milestone toward developing the chip. The next step of this research is to characterize the loss tangent of RO3450B. Then, a microwave-to-chip coupler to effectively insert microwaves onto a chip made from AlN is to be developed in order to apply the dielectric constant and loss tangent measurement methods to aluminum nitride. Finally, using the results of this research, fabrication and testing of the microwave atom trap chip itself will begin.

List of Figures

1.1	Image depicting 2-qubit gate behavior created by a spin-specific microwave atom trap chip, adapted from a talk given by Seth A. Aubin in 2018. Both qubits are initially in the spin-up state, separated in space. Qubit 1 is put in the spin-down state, then spatially moved near qubit 2 using the spin-specific force from the chip, creating interaction between the two qubits. Both qubits then pick up a phase because of this that can be measured, leading to two-qubit gate behavior.	2
2.1	Image depicting a 3 microstrip trace atom trap, adapted from [2]. In-phase microwave currents are sent through the two outer traces while a 180° out-of-phase microwave current is sent through the center trace. This will create an overall magnetic field with a minimum indicated by the arrow, which is used as the atom trap. Finally, a standing wave is created on the middle trace to create axial confinement of the atoms.	5
2.2	Plot of eigenenergies E_{\pm} of the dressed atom model versus the detuning δ/Ω .	7
2.3	Plot depicting the AC Zeeman energy shift.	8
2.4	Energy diagram showing the AC Zeeman effect. Negative detuning ($\delta < 0$) creates a larger energy gap between the two states, which allows the excited state $ \uparrow\rangle$ atoms to be trapped. Positive detuning ($\delta > 0$) creates a smaller energy gap, allowing the ground state $ \downarrow\rangle$ atoms to be trapped. Figure adapted from Miyahira et al, as presented at DAMOP Conference 2021. . . .	9

2.5	Image depicting setup of atom interferometry, adapted from a talk given by Seth A. Aubin in 2018. Each atom is put into a superposition of spin-up and spin-down with a $\pi/2$ pulse, then a spin-dependent force from the microwave atom chip is applied to separate the spin components. The spin states are then recombined with another $\pi/2$, creating an interference pattern allowing for precision measurements.	10
2.6	Image depicting a two-gap Fabry-Perot resonator. The gaps in the trace have reflective boundaries that create resonances. L describes the length between the cavities.	11
2.7	Example plot of resonances for a two-gap resonator illustrating the distance between the resonances Δf and the width of the resonances δf	12
3.1	Simple diagram depicting a parallel-plate capacitor with the capacitance meter. The two substrates of interest in this experiment are AlN and Rogers RO4350B.	15
3.2	Parallel-plate capacitors made from aluminum nitride CPWs showing (a) a top-down view depicting length l and width w and (b) a cross-section view showing the distance d between the copper plates.	16
3.3	Parallel-plate capacitor 1 made from Rogers RO4350B substrate showing (a) a top-down view depicting length l and width w and (b) a cross-section view showing the distance d between the copper plates.	17
3.4	Parallel-plate capacitor 2 made from Rogers RO4350B substrate showing (a) a top-down view depicting length l and width w and (b) a cross-section view showing the distance d between the copper plates.	18
3.5	Thick middle resonator: Utilizes a larger trace in the middle to create cavities	19
3.6	Reflection coefficient vs. frequency for the thick middle resonator of figure 3.5	20

3.7	Resonator Models in Sonnet. (a) makes use of 50 Ω microstrip trace with a small gap in the middle, (b) includes two gaps on the far end of either side of the 50 Ω trace, (c) uses a 50 Ω trace with a small vertical chapter (stub) in the middle, and (d) makes use of two of these stubs located 1/3 of the trace length in on either side.	21
3.8	Zoom in on the gap of the one-gap resonator in figure 3.7a	22
3.9	Reflection coefficient vs. frequency for the one-gap resonator of figure 3.7a.	22
3.10	Reflection coefficient vs. frequency for two-gap resonator of figure 3.7b.	23
3.11	Reflection coefficient vs. Frequency for one-stub resonator of figure 3.7c.	24
3.12	Reflection coefficient vs. Frequency for two-stub resonator of figure 3.7d.	25
3.13	HFSS model of Rogers RO4350B two-gap resonator	25
3.14	HFSS model of two-gap resonator as viewed from the bottom, showing the copper ground plane	26
3.15	HFSS model of two-gap resonator as viewed from the top, showing the gaps and dimensions of all major parts of the model	26
3.16	HFSS Simulation of the reflection coefficient (s11) vs. frequency for 2-gap Rogers resonator of figure 3.13.	27
3.17	Macroscopic Image of Rogers resonators. The one-gap resonator is on the top and the two-gap resonator is on the bottom. Zoomed in images of the gaps are shown in figures 3.18 and 3.19.	28
3.18	x35 magnification and measurement of the gap of the one-gap resonator.	29
3.19	x35 magnification and measurement of the gaps of the two-gap resonator.	30
3.20	Experimental results obtained from the VNA for the reflection coefficient (s11) vs. Frequency for 1-gap Rogers resonator of figure 3.17.	31
3.21	Experimental results obtained from the VNA for the reflection coefficient (s11) vs. Frequency for 2-gap Rogers resonator of figure 3.17.	32

3.22	Sonnet Simulation of reflection coefficient vs. frequency for 2-gap Rogers resonator with $\epsilon_r = 3.66$ compared to experimental data, from figures 3.7a and 3.17, respectively.	33
3.23	Sonnet Simulation of Reflection coefficients vs. Frequency for 2-gap Rogers resonator with $\epsilon_r = 3.77$, from figures 3.7b and 3.17, respectively.	34
3.24	Sonnet Simulation of Reflection coefficients vs. Frequency for a variety of loss tangent values. ϵ_r is kept constant at 3.77 for the model of figure 3.7a. . . .	35
4.1	Circuit used for power testing experiment with a microstrip	37
4.2	Qualitative plots depicting what the voltage plot will look like if the sample (a) can handle the current or (b) cannot handle the current and will break. Before the current source is turned on, the voltage will remain at zero and jump when the source is turned on.	38
4.3	CPW Schematics showing differences in trace width and gap width, designed in and adapted from [7]. (a) features gap widths of 2 mm and a trace width of 1 mm, while (b) features gap widths of 0.1 mm and a trace width of 0.2 mm	39
4.4	Voltage vs. time for 15A current through a CPW with a 1 mm width trace on AlN.	41
4.5	Voltage vs. time for a 15A current through a microstrip with a 0.41 mm width trace on AlN.	42
5.1	Dektak Scan of the Cu surface of 15 mm Al-Cu-AlN with scan length of 10 mm	45
5.2	HIROX images showing the edge and corner of sample A of 15 mm Cu-AlN-Cu. (a) shows a x400 magnification of the edge of the sample and (b) shows a x200 magnification of the corner.	47
5.3	HIROX images of 15 mm Cu-AlN-Cu. (a) shows a x200 magnification of the corner of sample B and (b) shows a x200 magnification of the edge of sample C.	48

5.4	HIROX images with x140 magnification of the cross-section of sample A of 15 mm Cu-AlN-Cu. (a) shows the left edge, (b) shows the right edge, and (c) shows the middle of the cross-section.	49
5.5	HIROX image with x100 magnification showing a defect in the cross-section of sample B of 15 mm Cu-AlN-Cu.	50
5.6	HIROX image with x200 magnification showing the edge of sample B of 22 mm Cu-AlN-Cu.	50
5.7	HIROX image with x200 magnification showing a defect in the cross-section of 22 mm Cu-AlN-Cu.	51
5.8	HIROX images of 15 mm Cu-Alumina-Cu. (a) shows a x400 magnification of the corner of sample B and (b) shows a x400 magnification of the edge of sample B.	51
5.9	HIROX images with x200 magnification of the cross-section of sample A of 15 mm Cu-Alumina-Cu. (a) shows the left edge, (b) shows the right edge, and (c) shows the middle of the cross-section.	52
5.10	HIROX images with x200 magnification of the cross-section of sample A of 22 mm Cu-Alumina-Cu. (a) shows the left edge, (b) shows the right edge, (c) shows the middle, and (d) shows a dip in the uppermost copper plane. . . .	53

List of Tables

3.1	Dimensions of the capacitors made of AlN from circuits	15
3.2	Measurements of C and D , and calculated ϵ_r for AlN Capacitor 1	16
3.3	Measurements of C and D , and calculated ϵ_r for AlN Capacitor 2	16
3.4	Dimensions of the Capacitors Made of RO4350B Substrate	17
3.5	Measurements of C and D , and calculated ϵ_r for RO4350B Capacitor 1	17
3.6	Measurements of C and D , and calculated ϵ_r for RO4350B Capacitor 2	18
3.7	Comparison of resonance spacing for 2-gap resonator models with different dielectric constants	29
5.1	Measurements of P_a and P_q from the Dektak profilometry of the Cu surface of the 15 mm Cu-AlN-Cu Sample	44
5.2	Measurements of P_a and P_q from the Dektak profilometry of the Cu surface of the 15 mm Cu-Alumina-Cu Sample	45
5.3	Measurements of P_a and P_q from the Dektak profilometry of the Cu surface of the 22 mm Cu-AlN-Cu Sample	46
5.4	Measurements of P_a and P_q from the Dektak profilometry of the Cu surface of the 22 mm Cu-Alumina-Cu Sample	46
5.5	Average P_a and P_q of all samples, summary of tables 5.1, 5.2, and 5.3, 5.4.	46

Chapter 1

Introduction

1.1 Motivation

The objective of this project is to characterize materials to be used in developing a microwave atom chip for trapping ultracold atoms. There are two major thrusts for the application of this atom chip: (1) cold-atom applications, and (2) quantum computing applications. Both of these applications rely on creating a spin-specific trap, which can be generated via the AC Zeeman effect with a microwave magnetic field with a local minimum. This minimum can be sculpted with the combined microwave near fields of several microstrip transmission lines.

For the cold-atom thrust, the main application is to trap ultracold thermal bosons or a Bose-Einstein Condensate in a spin-specific manner. Notably, spin-specific traps can be used as the basis for a spin-dependent atom interferometer. Such a matter wave interferometer is significantly more sensitive to gravity, electric fields, magnetic fields, and inertial forces than its optical counterpart.

For quantum computing applications, the spin of an atom is a 2-level system often used as a qubit in quantum information systems. Thus, being able to trap atoms in a spin-specific manner and spatially separate them has a significant advantage. For example, 2 traps can

be created for 2 separate qubits initially in the spin-up state. A 1-qubit gate can be acted on the first qubit to put it in a spin-down state, then that qubit can be spatially moved toward the second qubit, as shown in figure 1.1. This creates an interaction between the two qubits which then pick up a phase, creating 2-qubit gate behavior.

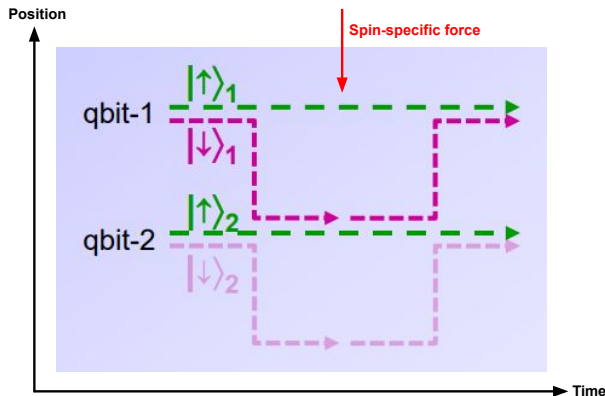


Figure 1.1: Image depicting 2-qubit gate behavior created by a spin-specific microwave atom trap chip, adapted from a talk given by Seth A. Aubin in 2018. Both qubits are initially in the spin-up state, separated in space. Qubit 1 is put in the spin-down state, then spatially moved near qubit 2 using the spin-specific force from the chip, creating interaction between the two qubits. Both qubits then pick up a phase because of this that can be measured, leading to two-qubit gate behavior.

1.2 Structure of Thesis

This thesis first outlines the relevant theory for this project in chapter 2, first going into atom trap theory and its application to atom interferometry, then discussing the theory for cavities and capacitors to inform later chapters. Chapter 3 discusses different approaches to measure the dielectric constant ϵ_r and loss tangent $\tan(\delta)$ of aluminum nitride (AlN) as well as experimental results completed on a different substrate with well-known properties, Rogers RO4350B, to provide proof-of-concept. Chapter 4 discusses experiments done to characterize the maximum current that the chip will be able to handle.

To apply the ideas outlined in chapter 3 to AlN, rectangular samples of aluminum nitride sandwiched between two copper planes were ordered. In order to use these samples, they

must be smooth and of high-quality. Therefore, the surface roughness and quality of the samples are discussed in [chapter 5](#).

Chapter 2

Theory

This chapter describes the basic theory of AC Zeeman chip traps in section 2.1 and atom interferometry in section 2.2. Then to inform later work in the thesis, the chapter also reviews the theory of microstrip “Fabry-Perot” cavities in section 2.3 and finally dielectric capacitors in section 2.4.

2.1 Atom trap theory

The focus of the Aubin lab is to create a spin-specific atom trap chip for atom interferometry. This chapter describes the theory behind the atom trap, beginning with a basic overview of a microwave atom chip, then AC Zeeman theory and finally going into dressed atom theory. After describing how the chip works and can trap atoms with a specific spin, an application of this work will be described: atom-based interferometry.

The chip will make use of three microstrip transmission lines to generate a trap as shown in figure 2.1. In-phase microwave currents will be sent through the two outer traces, creating an overall microwave magnetic field. By directing 180° out-of-phase microwaves through the center trace, the combined microwave magnetic field will have a minimum, indicated by the arrow. This minimum can be used to trap atoms as described in section 2.1.1. A standing wave, generated by directing counter-propagating microwaves on the center trace, results in

a microwave lattice for axial confinement of atoms along the length of the trace.

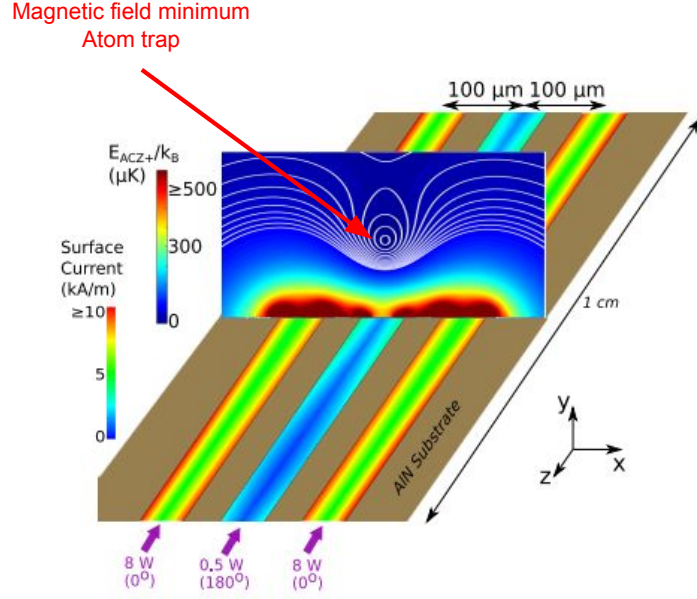


Figure 2.1: Image depicting a 3 microstrip trace atom trap, adapted from [2]. In-phase microwave currents are sent through the two outer traces while a 180° out-of-phase microwave current is sent through the center trace. This will create an overall magnetic field with a minimum indicated by the arrow, which is used as the atom trap. Finally, a standing wave is created on the middle trace to create axial confinement of the atoms.

2.1.1 AC Zeeman Effect

Consider an atom with 2 spin states, $|g\rangle$ and $|e\rangle$ with energies E_g and E_e , respectively, with $E_e > E_g$. In the far-detuned limit (near the center of the trap), the transition amplitude (also called the Rabi frequency) is given by:

$$\Omega = \frac{\langle g | H_{Zeeman} | e \rangle}{\hbar} \quad (2.1)$$

where the Zeeman Hamiltonian for a two-level spin system is given by $H_{Zeeman} = -\vec{\mu} \cdot \vec{B}_{AC}$, with $\vec{\mu}$ being the magnetic moment and \vec{B}_{AC} being the AC Zeeman field. These spin states

are separated by an energy E corresponding to a frequency ω_{ge} given by $\omega_{ge} = \Delta E/\hbar$. The microwave field \vec{B}_{AC} corresponds to a frequency ω_{AC} . The difference between the microwave frequencies and that of the spin states is known as the detuning $\delta = \omega_{AC} - \omega_{ge}$. When this detuning is added to the system, the energy levels will shift. One method of solving for this energy shift is using the dressed atom approach as described in section 2.1.2.

2.1.2 Dressed Atom Theory

In order to solve for the energy shift created from the detuning, the wavefunction of the system evolves according to equation 2.2 must be solved.

$$-i\hbar \frac{\partial}{\partial t} |\psi\rangle = H_o |\psi\rangle - \vec{\mu} \cdot \vec{B}_{AC} \cos(\omega_{AC}t + \theta) \quad (2.2)$$

where H_o is the Hamiltonian of the atom. The dressed atom approach simplifies this equation. The microwave magnetic field applied, \vec{B}_{AC} , contains N photons. Thus the system has a ground state with N photons and an excited state with $N-1$ photons as it took one photon to excite the atom, giving us our basis: $\{|g, N\rangle, |e, N-1\rangle\}$.

The Hamiltonian of our system is then given by three components: one term from the atom, one term for the microwave field (shortened to AC field in the following), and one from the interaction between the two:

$$H = H_{atom} + H_{ACfield} + H_{interaction} \quad (2.3)$$

$$= \hbar\omega_{ge} \begin{bmatrix} 0 & 0 \\ 0 & 1 \end{bmatrix} + \hbar\omega_{AC} \begin{bmatrix} N & 0 \\ 0 & N-1 \end{bmatrix} + \frac{\hbar}{2} \begin{bmatrix} 0 & \Omega \\ \Omega^* & 0 \end{bmatrix} \quad (2.4)$$

where $\omega_{ge} = \omega_e - \omega_g$. Equation 2.4 can then be further simplified by introducing a constant energy offset of $E_0 = \hbar\omega_{AC}N + \hbar\frac{\delta}{2}$, where δ is the detuning given by $\delta = \omega_{AC} - \omega_{ge}$. This has the effect of subtracting E_0I from the Hamiltonian, where I is the identity matrix, resulting in the final dressed atom Hamiltonian given by equation 2.5:

$$H = \frac{\hbar}{2} \begin{bmatrix} -\delta & \Omega \\ \Omega & \delta \end{bmatrix} \quad (2.5)$$

The Hamiltonian can then be diagonalized to find the eigenenergies, given in equation 2.6 and plotted in figure 2.2:

$$E_{\pm} = \pm \frac{\hbar}{2} \sqrt{\delta^2 + \Omega^2} \quad (2.6)$$

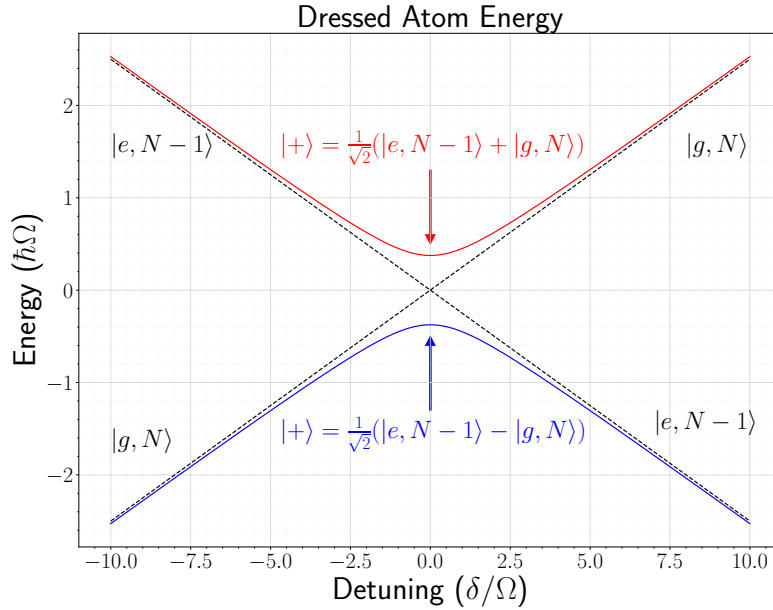


Figure 2.2: Plot of eigenenergies E_{\pm} of the dressed atom model versus the detuning δ/Ω .

Figure 2.2 depicts the dressed atom energies versus the detuning δ/Ω (i.e. detuning δ is in units of Ω). The positive state $|+\rangle$ is shown in red while the negative state $|-\rangle$ is shown in blue. The bare atom and photon states (without the interaction term of the Hamiltonian) are shown in black. Then, by subtracting the dressed atom energy from the bare energy, we arrive at the AC Zeeman energy shift as given in equation 2.7:

$$\Delta E_{\pm} = \pm \frac{\hbar}{2} (\sqrt{|\Omega|^2 - \delta^2} - |\delta|) \quad (2.7)$$

As shown in figure 2.3, The positive $|+\rangle$ state (shown in red) has a positive energy shift, so it becomes a low-field seeker while the negative $|-\rangle$ state (shown in blue) has a negative energy shift, so it becomes a high-field seeker.

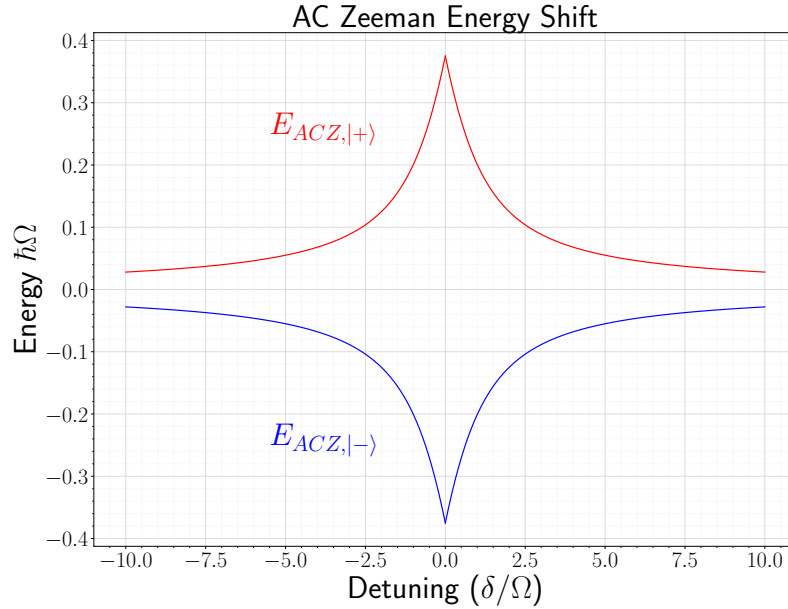


Figure 2.3: Plot depicting the AC Zeeman energy shift.

By taking the far-detuned limit of equation 2.7 ($|\delta| \gg |\Omega|$), the energy level shift can be simplified to equation 2.8:

$$\Delta E_{\pm} \approx \pm \frac{\hbar \Omega^2}{4 \delta} \quad (2.8)$$

The energy shift in this limit is shown in figure 2.4. This figure shows how the magnetic field minimum of the trap can be used to trap atoms in a spin specific manner: if the detuning is negative, the energy of the ground state $|g\rangle$ will decrease while the excited state $|e\rangle$ will increase energy. An atom will tend to a configuration with the lowest energy, so the ground state will now seek a higher microwave field (high-field seeker) and the excited state will

seek a lower microwave field (low-field seeker). For a positive detuning, the reverse happens: $|g\rangle$ becomes a low-field seeker and $|e\rangle$ becomes a high-field seeker. Since our trap utilized a magnetic field minimum, the low-field seekers will be attracted to the trap and the high-field seekers will be repelled from it. Thus, changing the detuning to be positive or negative dictates whether excited states or ground states are trapped.

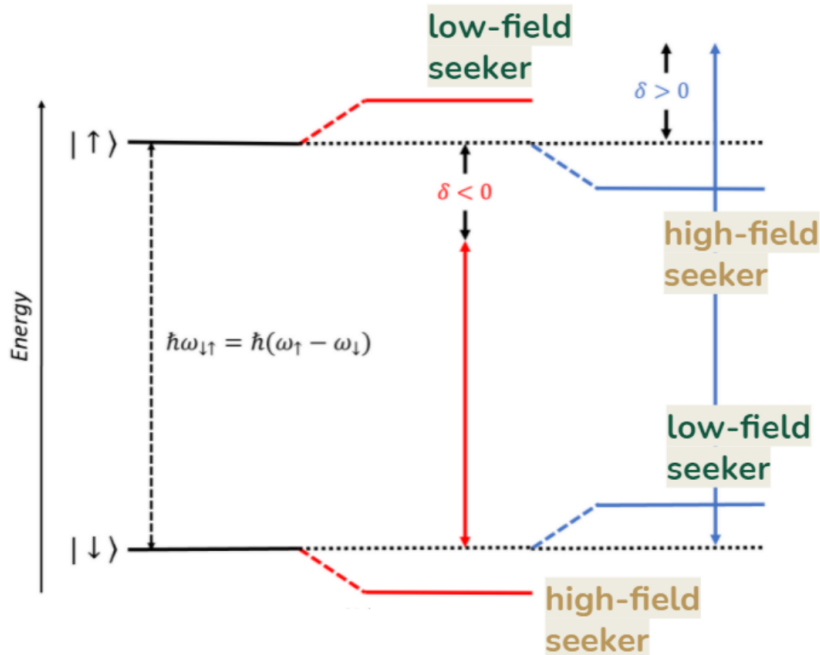


Figure 2.4: Energy diagram showing the AC Zeeman effect. Negative detuning ($\delta < 0$) creates a larger energy gap between the two states, which allows the excited state $|\uparrow\rangle$ atoms to be trapped. Positive detuning ($\delta > 0$) creates a smaller energy gap, allowing the ground state $|\downarrow\rangle$ atoms to be trapped. Figure adapted from Miyahira et al, as presented at DAMOP Conference 2021.

2.2 Atom Interferometry

As described in chapter 1.1, atom interferometry has many benefits over its optical counterpart. An atom-based interferometer can be configured analogously to an optical Mach-Zehnder interferometer, which uses the interference pattern of light to make precision measurements. To utilize atoms in a similar way, they must behave in a wave-like manner, thus

requiring a Bose-Einstein Condensate (BEC) or ultracold thermal bosons. Each atom is put into a superposition of spin-up and spin-down using a $\pi/2$ pulse, then a spin-dependent force is applied to separate the two spin components of the atom. The microwave atom chip provides a microwave magnetic near field that generates a spin-specific force via the AC Zeeman effect as described in chapter 2.1. The spin states are then recombined with another $\pi/2$ pulse, creating an interference pattern that allows precision measurements to be made. The basic layout for the interferometer is depicted in figure 2.5.

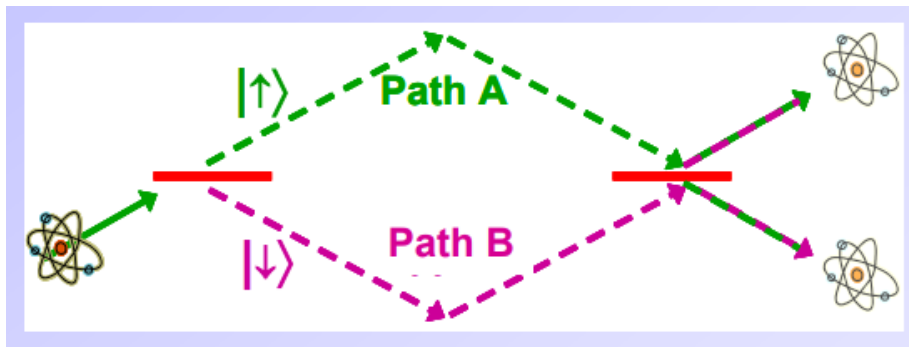


Figure 2.5: Image depicting setup of atom interferometry, adapted from a talk given by Seth A. Aubin in 2018. Each atom is put into a superposition of spin-up and spin-down with a $\pi/2$ pulse, then a spin-dependent force from the microwave atom chip is applied to separate the spin components. The spin states are then recombined with another $\pi/2$, creating an interference pattern allowing for precision measurements.

2.3 Cavity Theory

A large part of the research in this thesis involved measuring the properties of the substrate to be used in the chip, i.e. the material onto which the copper traces will be deposited. Notably, the dielectric constant and loss tangent are to be characterized. This section outlines the theory behind resonators and how they can be used to accomplish this.

A resonator is a device that oscillates at greater amplitudes at certain resonant frequencies. One such device is known as a Fabry-Perot cavity resonator, in which there is a hollow space in the device with reflective boundaries that creates those resonances. One of the simplest cavity resonators is a simple microstrip of metal on a substrate with two gaps

in the trace (two-gap resonator), as shown in figure 2.6. When electromagnetic waves are sent through one end of the trace, the gaps act as "mirrors" and reflect the wave back and forth. This continuous reflection creates constructive or destructive interference, which is what gives the sharp amplitude spikes at the resonant frequencies. Figure 2.7 provides an example of a resonance plot from a simulation as described in section 3.2.

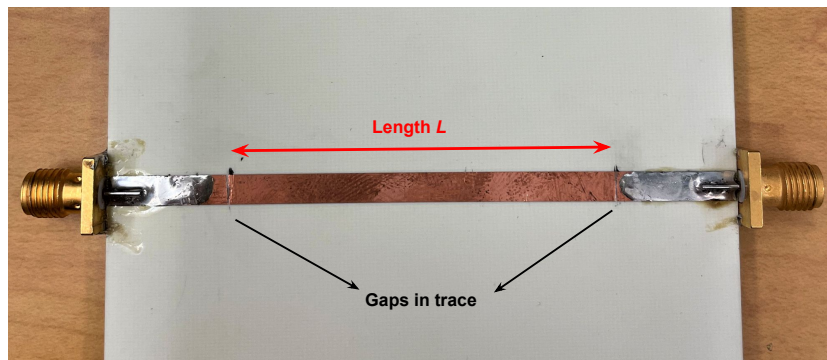


Figure 2.6: Image depicting a two-gap Fabry-Perot resonator. The gaps in the trace have reflective boundaries that create resonances. L describes the length between the cavities.

The distance between the resonances (Δf), called the free spectral range (FSR), is related to the length L of the middle trace by the following relation:

$$\Delta f = \frac{v}{2L} \quad (2.9)$$

where v is the speed at which the wave is traveling. Electromagnetic waves travel at the speed of light c in a vacuum, but since the wave is in a medium, the speed of travel will be lessened by the medium's index of refraction n_{eff} :

$$v = \frac{c}{n_{eff}} \quad (2.10)$$

Here, n_{eff} is approximately related to the relative dielectric constant $\epsilon_{r,eff}$ of the material

by the following:

$$n_{eff} \approx \sqrt{\epsilon_{r,eff}} \quad (2.11)$$

This approximation is true whenever the magnetic permeability $\mu \approx \mu_0$, which is true for most materials including the ones used in this research. Here, $\epsilon_{r,eff}$ is the *effective* dielectric constant, dependent on the geometry of the microstrip transmission line. It is related to the actual dielectric constant by

$$\epsilon_r = \alpha \epsilon_{r,eff} \quad (2.12)$$

where α is a constant of proportionality that depends on the geometry of the microstrip transmission line and must be calculated from simulations. Finally, putting equations 2.9, 2.10, 2.11, and 2.12 together leads to the following equation for calculating the dielectric constant of the material:

$$\epsilon_r = \frac{1}{\alpha} \left(\frac{c}{2\Delta f} \right)^2 \quad (2.13)$$

The widths of the resonances δf are also important, as they are related in part to the loss tangent $\tan \delta$.

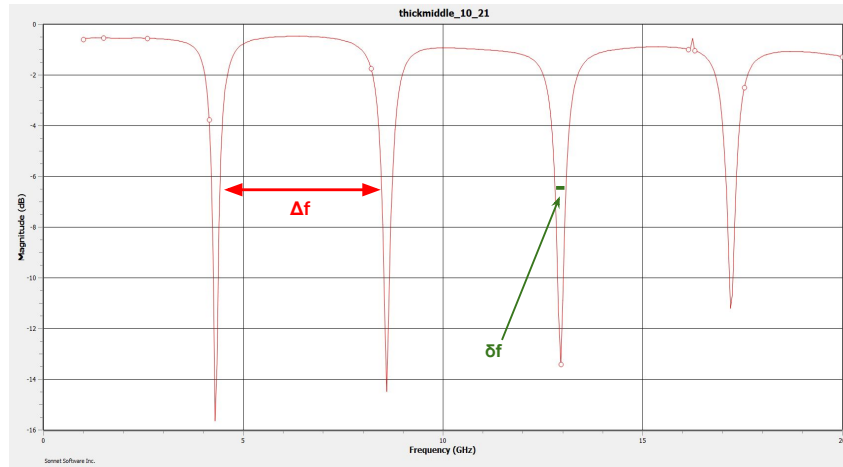


Figure 2.7: Example plot of resonances for a two-gap resonator illustrating the distance between the resonances Δf and the width of the resonances δf .

2.4 Parallel-plate Capacitor Theory

At near DC frequencies (i.e. GHz scale), the dielectric constant can also be measured by using its relation to the capacitance in a parallel-plate capacitor (see page 106 of [1]):

$$C = \epsilon_r \epsilon_0 \frac{A}{d} = \epsilon_r \epsilon_0 \frac{lw}{d} \quad (2.14)$$

where ϵ_r is the dielectric constant and $\epsilon_0 = 8.85 \times 10^{-12} \frac{C^2}{Nm^2} = 0.0085 \frac{pF}{mm}$ is the permittivity of free space. The capacitors used in this research are rectangular, so the area A of the plates can be defined in terms of the length l and the width w of the plates. Finally, d is the distance between the plates. Rearranging this equation leads to a formula for extracting the dielectric constant from a measurement of the capacitance and dimensions of the capacitor:

$$\epsilon_r = \frac{Cd}{\epsilon_0 lw} \quad (2.15)$$

Chapter 3

Measuring the Dielectric Constant and Loss Tangent of Aluminum Nitride

A typically accepted value of the dielectric constant of aluminum nitride (AlN) is $\epsilon_r = 8.8$ [3], but manufacturing variations cause this constant to have a “range”. The manufacturer of our AlN reports a range of between 8 and 10; since this will have a large bearing on the design of the atom trap chip, it is important to characterize this value exactly. There are 3 possible approaches: (1) construct a parallel-plate capacitor and extract the dielectric coefficient and loss tangent from the capacitance, (2) make a resonator and extract the dielectric constant from the spacing of the resonances and the loss tangent from their widths, and (3) create a standing wave along a microstrip and extract the dielectric constant. This thesis discusses approaches (1) and (2).

3.1 Parallel-plate Capacitor Approach

A simple way to measure the dielectric constant and loss tangent is to use a parallel-plate capacitor. Figure 3.1 depicts a simple diagram showing the approach: a capacitor is created

consisting of two copper plates with a substrate in the middle, then a capacitance meter is used to directly measure the capacitance C and loss tangent d ($\tan(\delta)$).

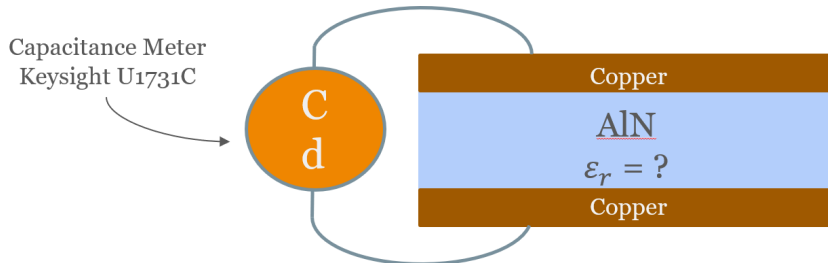


Figure 3.1: Simple diagram depicting a parallel-plate capacitor with the capacitance meter. The two substrates of interest in this experiment are AlN and Rogers RO4350B.

An AlN circuit from previous research [7] was modified by cutting away parts of the circuit and using the top and bottom ground planes of a co-planar waveguide (CPW) to make a capacitor, as shown in figure 3.2. The dimensions of these are given in table 3.1.

Capacitor Number	Length l (mm)	Width w (mm)	Distance d (mm)
1	28.07 ± 0.10	8.46 ± 0.02	0.88 ± 0.02
2	28.20 ± 0.03	5.56 ± 0.08	0.90 ± 0.02

Table 3.1: Dimensions of the capacitors made of AlN from circuits

A Keysight U1731C capacitance meter was then used, which has the ability to measure both the capacitance C and the loss tangent $d = \tan(\delta)$ at different frequencies. These measurements are shown in tables 3.2 and 3.3 along with the dielectric constants calculated from equation 2.15. These measurements are consistently higher than the reported value of the data sheet, so it is believed there is a systematic error in the capacitance meter/experimental setup. Thus, measurements of a well-characterized substrate, Rogers RO4350B, were taken to gauge how accurate this method is.

According to the datasheet for RO4350B, its dielectric constant is $\epsilon_r = 3.66$ and its loss tangent is $\tan(\delta) = 0.0037$ at $8 - 40$ GHz and 23°C [9]. To measure ϵ_r using this method, a

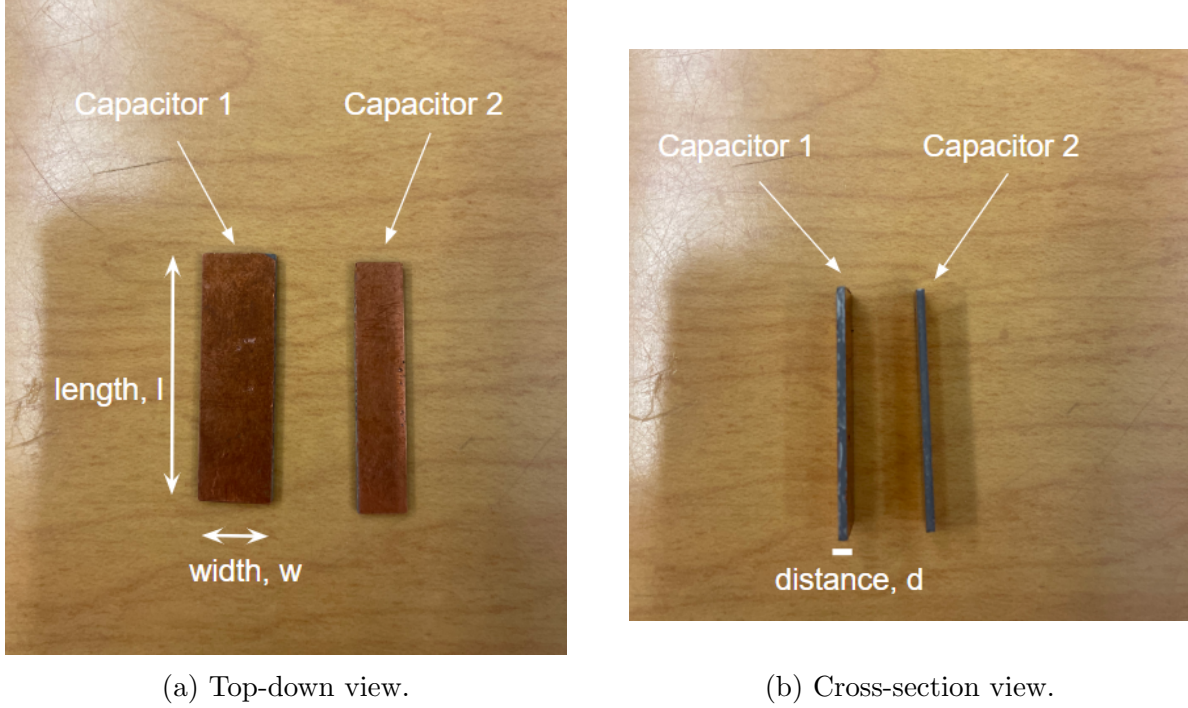


Figure 3.2: Parallel-plate capacitors made from aluminum nitride CPWs showing (a) a top-down view depicting length l and width w and (b) a cross-section view showing the distance d between the copper plates.

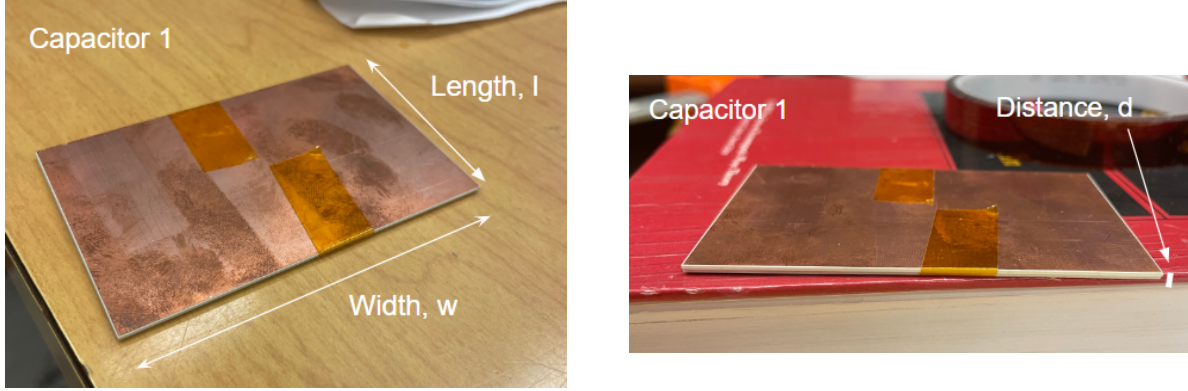
Frequency (Hz)	C_1 (pF)	$\epsilon_{r,1}$	$\tan(\delta)_1$
100	24.4 ± 0.5	10.2 ± 0.1	0.036 ± 0.005
120	24.2 ± 0.1	10.1 ± 0.1	0.080 ± 0.004
1000	22.9 ± 0.1	9.6 ± 0.1	0.035 ± 0.005

Table 3.2: Measurements of C and D , and calculated ϵ_r for AlN Capacitor 1

Frequency (Hz)	C_2 (pF)	$\epsilon_{r,2}$	$\tan(\delta)_2$
100	16.9 ± 0.4	10.9 ± 0.1	0.046 ± 0.005
120	18.1 ± 0.1	11.7 ± 0.1	0.096 ± 0.005
1000	15.9 ± 0.1	10.2 ± 0.1	0.036 ± 0.005

Table 3.3: Measurements of C and D , and calculated ϵ_r for AlN Capacitor 2

sheet of RO4350B with a thin layer of copper on top was cut in half, and then both halves were pressed together to create a parallel-plate capacitor. Two different setups were created; (1) one with a larger distance between the plates and a larger area shown in figure 3.3, and (2) another with a smaller distance and a smaller area shown in figure 3.4. The dimensions



(a) Top-down view.

(b) Cross-section view.

Figure 3.3: Parallel-plate capacitor 1 made from Rogers RO4350B substrate showing (a) a top-down view depicting length l and width w and (b) a cross-section view showing the distance d between the copper plates.

of these two setups are shown in table 3.4.

Capacitor Number	Distance d (mm)	Width w (mm)	Length l (mm)
1	1.53 ± 0.60	80.04 ± 0.06	50.45 ± 0.05
2	0.77 ± 0.02	50.50 ± 0.30	49.50 ± 0.30

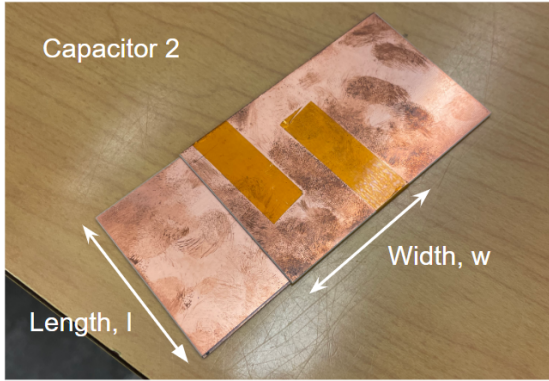
Table 3.4: Dimensions of the Capacitors Made of RO4350B Substrate

The capacitances and the loss tangents of the two capacitors were then measured at different frequencies, and then equation 2.15 was used to calculate the dielectric constants. The measurements and calculated values of ϵ_r are shown in tables 3.5 and 3.6, along with the percent by which the values differ from the ones reported on the data sheet.

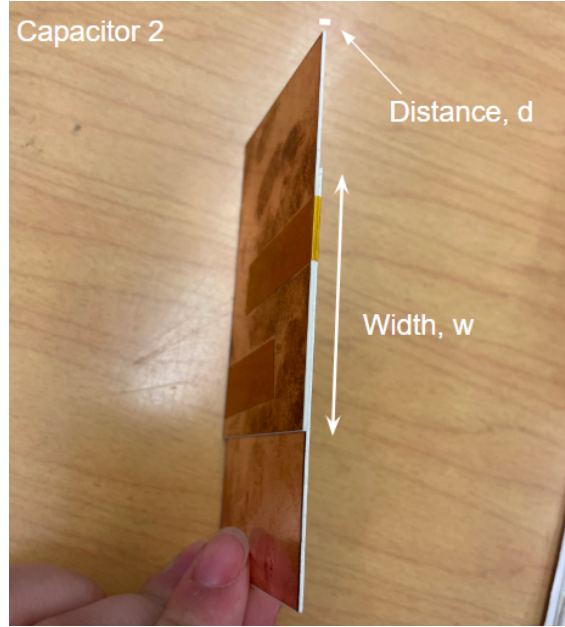
Frequency (Hz)	C_1 (pF)	$\epsilon_{r,1}$	% diff.	$\tan(\delta)_1$	% diff.
100	97.6 ± 0.3	4.35	17.23%	0.020 ± 0.010	137.55%
120	98.2 ± 0.3	4.37	17.75%	0.030 ± 0.010	156.08%
1000	95.68 ± 0.05	4.27	15.27%	0.030 ± 0.005	156.08%

Table 3.5: Measurements of C and D , and calculated ϵ_r for RO4350B Capacitor 1

Since the calculated values of ϵ_r are consistently higher than that of the data sheet (around 10% or higher), it was concluded that this method potentially results in values that are systematically higher than the true value. This is likely due to how the dielectric constant



(a) Top-down view.



(b) Cross-section view.

Figure 3.4: Parallel-plate capacitor 2 made from Rogers RO4350B substrate showing (a) a top-down view depicting length l and width w and (b) a cross-section view showing the distance d between the copper plates.

Frequency (Hz)	C_1 (pF)	$\epsilon_{r,1}$	% diff.	$\tan(\delta)_1$	% diff.
100	120 ± 10	4.20	15.57%	0.004 ± 0.002	7.79%
120	112 ± 1	4.06	10.43%	0.012 ± 0.005	105.73%
1000	111 ± 1	4.02	9.25%	0.008 ± 0.003	73.50%

Table 3.6: Measurements of C and D , and calculated ϵ_r for RO4350B Capacitor 2

changes with frequency; the Rogers Corporation defines their dielectric constant for a much higher frequency range ($8-40 \text{ GHz}$) than what was used in this experiment ($100 \text{ Hz}-1 \text{ kHz}$), as limited by our capacitance meter. The same can be said of the loss tangent $\tan(\delta)$, though there may be some inconsistency with the capacitance meter measurements since the percent differences are not consistent.

3.2 Resonator Approach

The second approach makes use of a resonator to extract the dielectric constant of AlN at microwave frequencies as explained in section 2.3. This experiment began with computer simulations to decide on the design of the resonator, then physical experimentation on the Rogers RO4350B substrate to verify the accuracy simulations.

3.2.1 Sonnet Simulations

The major hurdle for this approach was designing a resonator that would give us narrow enough resonances to find the dielectric constant. Five different designs were created using the Sonnet simulation software, as shown in figures 3.5 and 3.7.

The first design was a $50\ \Omega$ microstrip line that increased in width in the middle (wide section is not $50\ \Omega$) as shown in figure 3.5. This design was first studied in previous work by Stephen Rosene in his senior thesis project in the Aubin Lab [8]. Though this design has resonances (see figure 3.6), they are not narrow enough for measuring loss tangents less than 0.05.

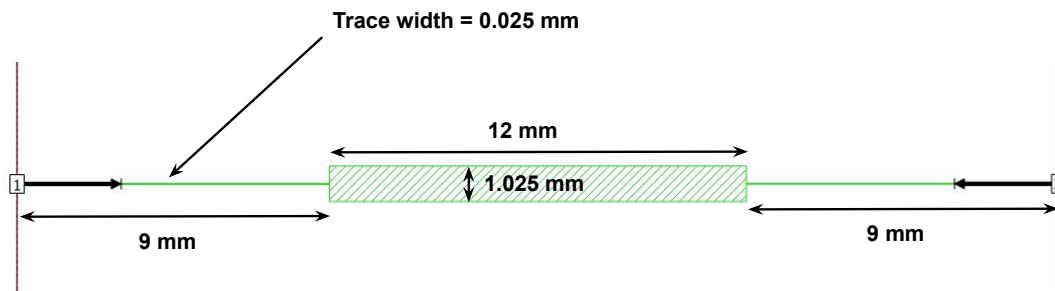


Figure 3.5: Thick middle resonator: Utilizes a larger trace in the middle to create cavities

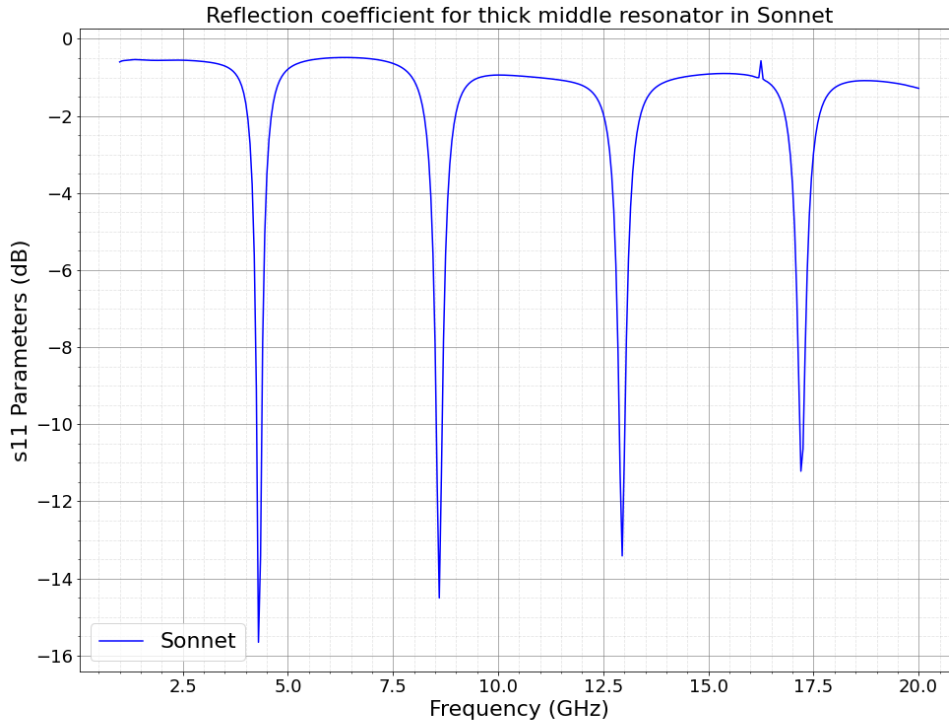
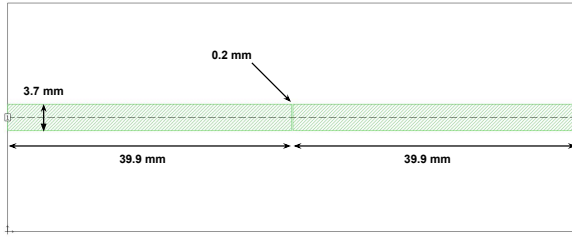


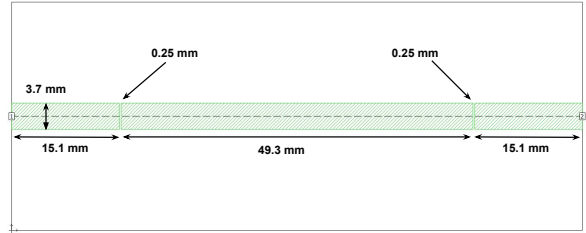
Figure 3.6: Reflection coefficient vs. frequency for the thick middle resonator of figure 3.5

The second and third designs used a $50\ \Omega$ microstrip line with one (figure 3.7a) or two (3.7b) small gaps in the trace. A zoom-in on the gap of figure 3.7a is shown in figure 3.8. The one-gap resonator gave some resonances at higher frequencies as shown in figure 3.9, but there are not enough resonances nor are they narrow enough for this experiment. The two-gap resonator, however, shows many narrow resonances across the entire frequency range, as shown in figure 3.10. This design is favorable because of these quality resonances as well as the ease of fabricating it. Creating a high-quality gap resonator simulation model proved to be non-trivial, so a few tips are given in Appendix D for future reference.

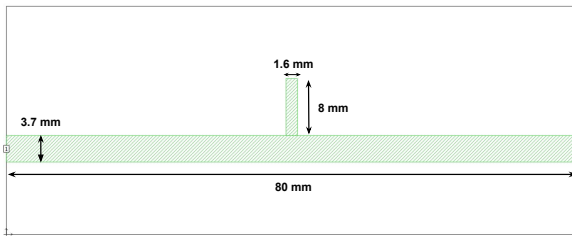
The third and fourth designs (figures 3.7c and 3.7d) are both variations of the well-known stub resonator. Both use a $50\ \Omega$ microstrip line connected to either one stub (one-stub resonator) or two stubs of the same thickness as the microstrip line (two-stub resonator). The results of the one- and two-stub resonators are shown in figures 3.11 and 3.12, respectively.



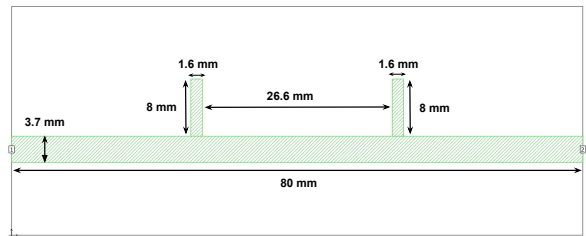
(a) One-Gap Resonator



(b) Two-Gap Resonator



(c) One-stub Resonator



(d) Two-stub Resonator

Figure 3.7: Resonator Models in Sonnet. (a) makes use of 50Ω microstrip trace with a small gap in the middle, (b) includes two gaps on the far end of either side of the 50Ω trace, (c) uses a 50Ω trace with a small vertical chapter (stub) in the middle, and (d) makes use of two of these stubs located $1/3$ of the trace length in on either side.

While there appear to be a few resonances around 10 GHz for both of these designs, they are not periodically spaced, so it would be difficult to extract the dielectric constant from the plots. Therefore, the two-gap resonator design was used moving forward by first verifying its performance with Ansys HFSS simulations, and then moving onto experimental tests.

3.2.2 Ansys HFSS Simulations

In order to verify the Sonnet results, a model of the two-gap resonator in Ansys HFSS with similar geometry to that of the physical setup was created, as shown in figures 3.13 - 3.15. The s11-parameters (i.e. reflection coefficient) in the $0 \text{ GHz} - 20 \text{ GHz}$ range are shown in figure 3.16. HFSS is a more powerful modeling software as it is a three-dimensional solver

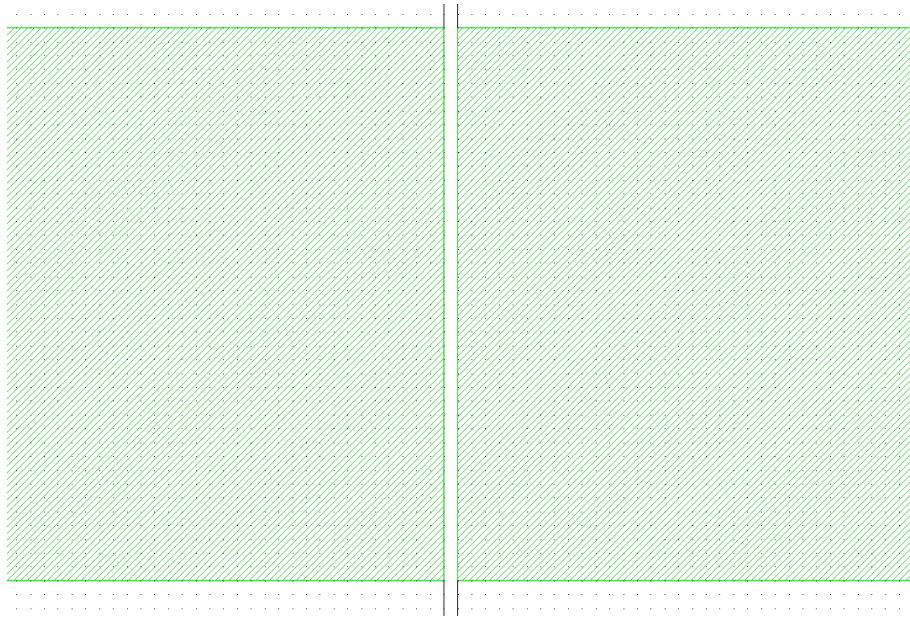


Figure 3.8: Zoom in on the gap of the one-gap resonator in figure 3.7a



Figure 3.9: Reflection coefficient vs. frequency for the one-gap resonator of figure 3.7a.

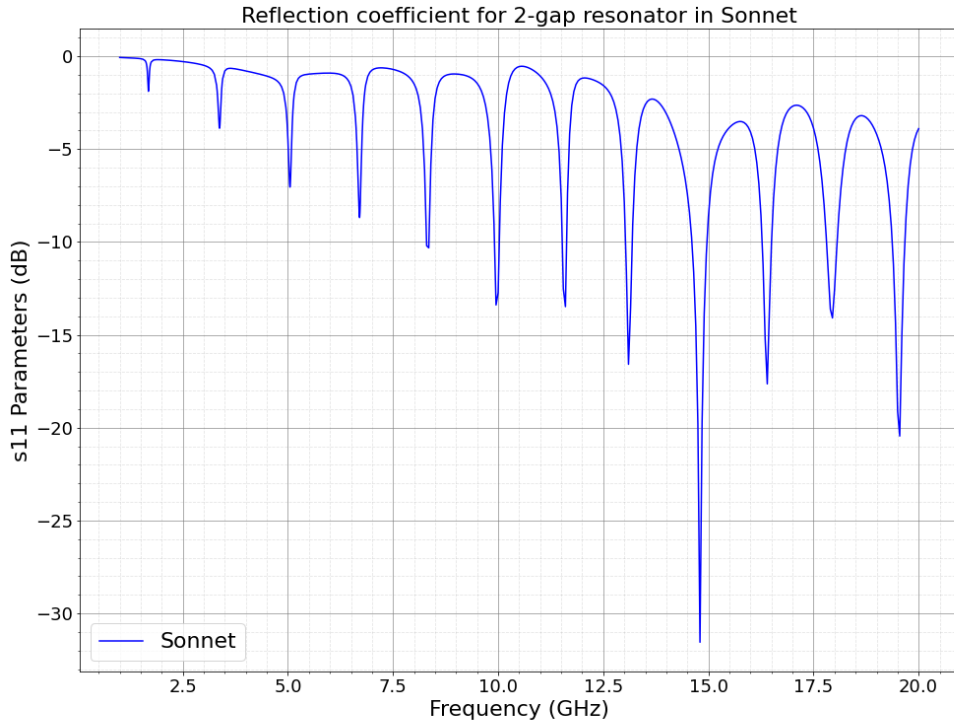


Figure 3.10: Reflection coefficient vs. frequency for two-gap resonator of figure 3.7b.

whereas Sonnet is only a two-dimensional one, but Sonnet allows for much quicker solutions and is easier to use. Since the results of both software are comparable, Sonnet was used moving forward.

3.2.3 Experimental Results

Finally, an experimental test was performed to extract the dielectric constant. A resonator was created using a microstrip consisting of a copper trace (thickness = $35 \mu m$, width = $3.7 mm$) on a Rogers RO4350B substrate (thickness = $1.524 \mu m$). As stated in section 3.1, RO4350B has a relative dielectric constant of $\epsilon_r = 3.66$ and a loss tangent of $\tan(\delta) = 0.0037$. Two resonators were created by removing small gaps of copper from the trace: (a) a one-gap resonator and (b) a two-gap resonator. The macroscopic view is shown in figure 3.17 while zoomed-in views of the gaps are shown in figures 3.18 and 3.19.

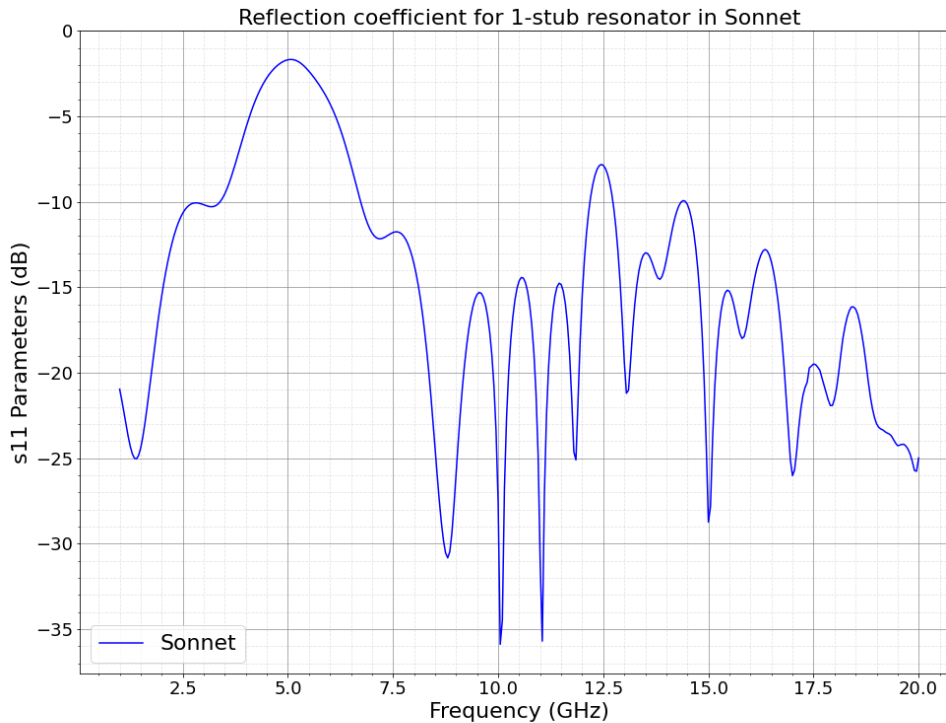


Figure 3.11: Reflection coefficient vs. Frequency for one-stub resonator of figure 3.7c.

These resonators were then connected to an Anritsu MS2038C Vector Network Analyzer (VNA), which allowed us to measure the reflection coefficient (s11-parameter), as shown in figures 3.20 and 3.21. The one-gap resonator showed periodic resonances in the higher frequencies, but the two-gap resonator showed many more periodic and narrower resonances in the entire frequency range, verifying that this is the resonator model that will work best for measuring the dielectric constant. The Python code snippet in Appendix A shows how the plots were created and the snippet in Appendix B shows how the resonances were found. The experimental data was very comparable to the simulation data, so the next step was to extract the dielectric constant and loss tangent of RO3450B as described in sections 3.2.4 and 3.2.5, respectively.

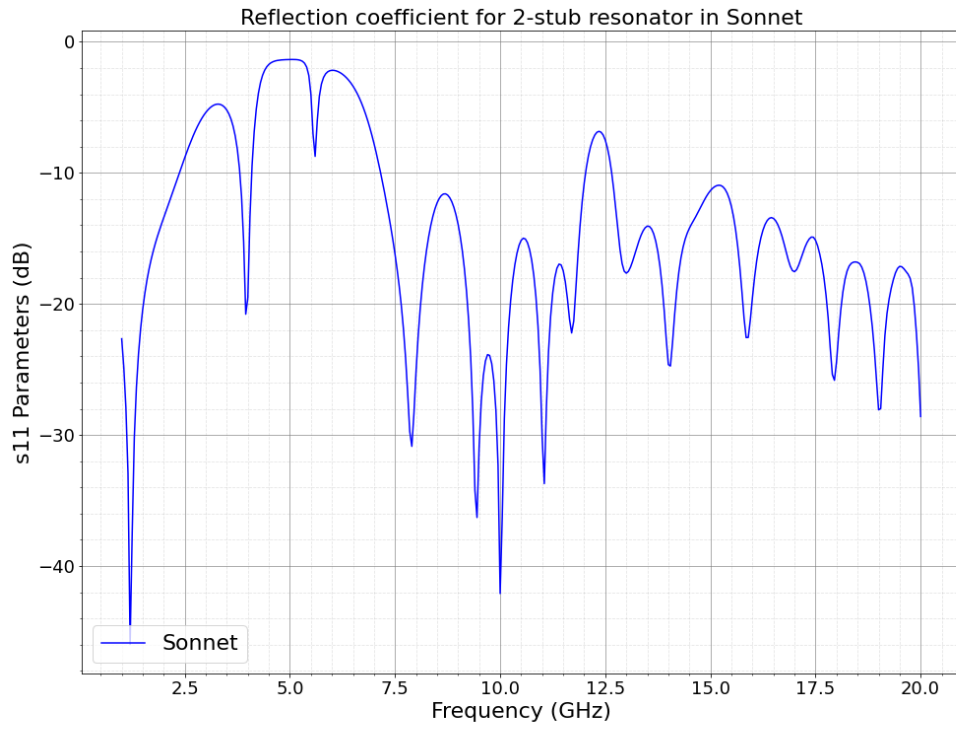


Figure 3.12: Reflection coefficient vs. Frequency for two-stub resonator of figure 3.7d.

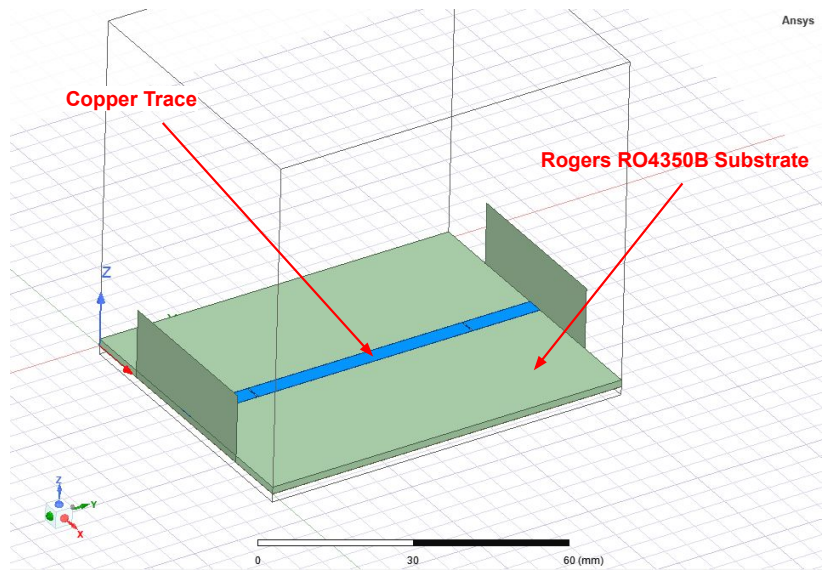


Figure 3.13: HFSS model of Rogers RO4350B two-gap resonator

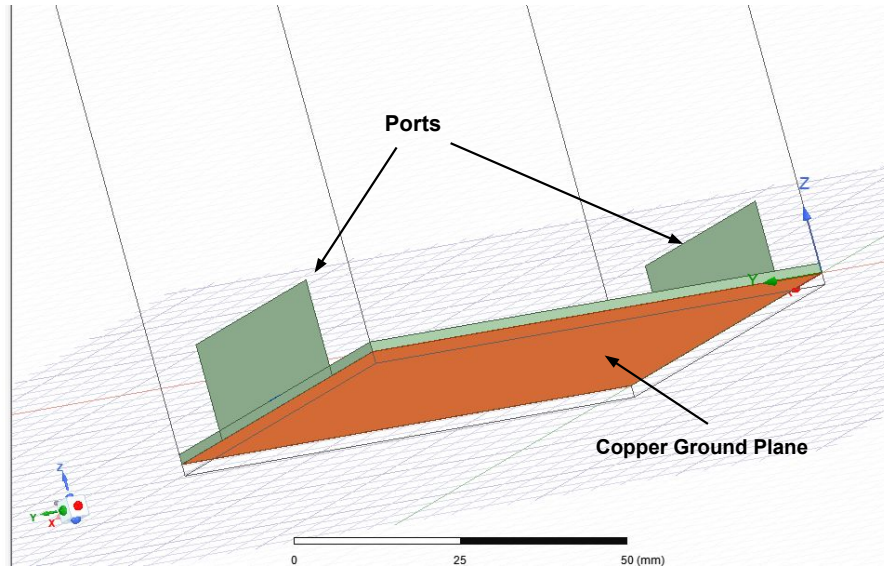


Figure 3.14: HFSS model of two-gap resonator as viewed from the bottom, showing the copper ground plane

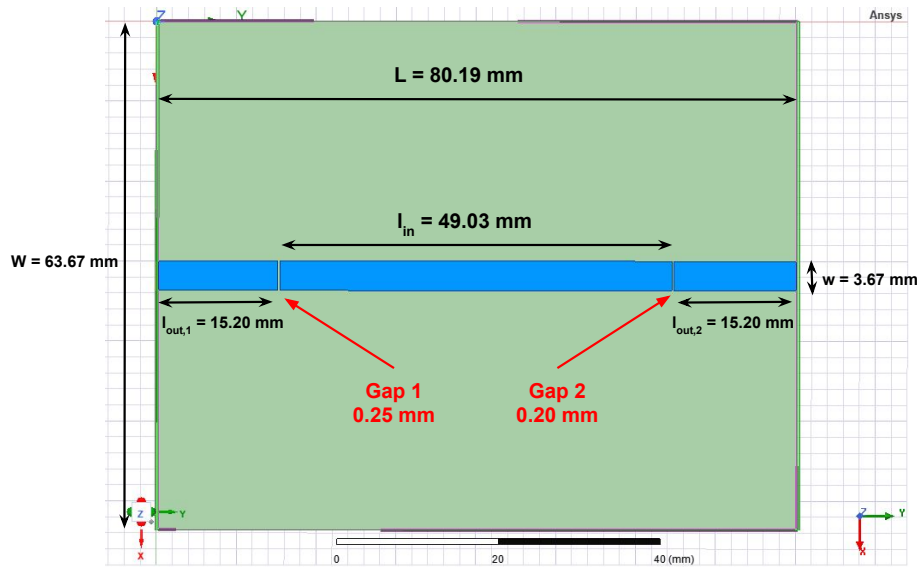


Figure 3.15: HFSS model of two-gap resonator as viewed from the top, showing the gaps and dimensions of all major parts of the model

3.2.4 Extracting the Dielectric Constant

The link between the dielectric constant ϵ_r and the spacing between the resonant frequencies are given by equation 2.13 in section 2.3 on cavity theory. Equation 2.13 includes a constant of proportionality α dependent on the geometry, which can be extracted from simulations.

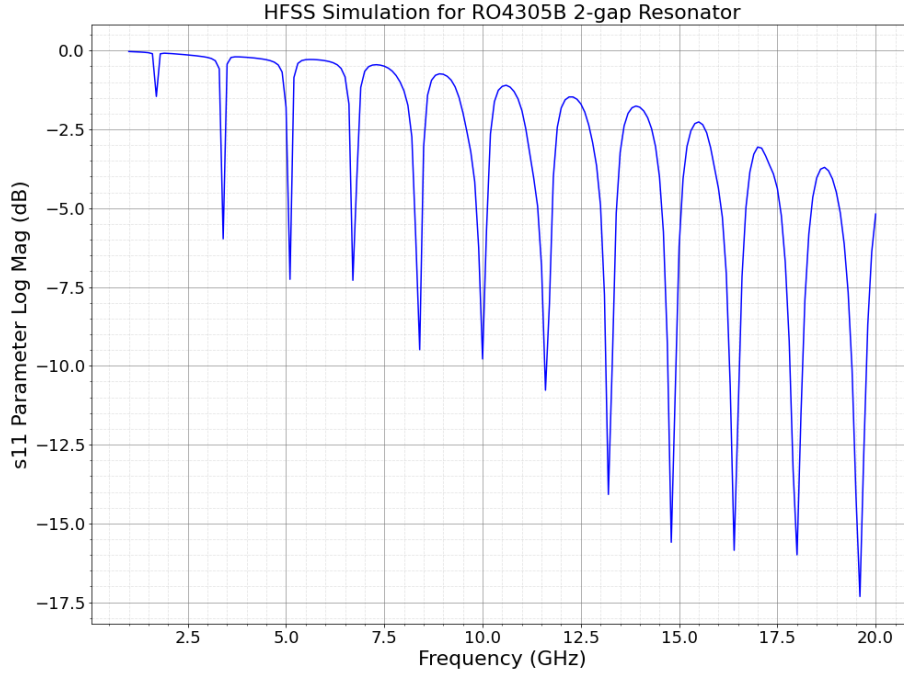


Figure 3.16: HFSS Simulation of the reflection coefficient (s11) vs. frequency for 2-gap Rogers resonator of figure 3.13.

However, since ϵ_r and $\tan(\delta)$ of the material can be changed directly in the simulation software, the experimental data and simulation data for a variety of different ϵ_r and $\tan(\delta)$ values can simply be compared until the simulation matches the experimental data. As outlined in chapter 2.3, the dielectric constant is related to the spacing of the resonances while the loss tangent is related to the width of those resonances, so those are the two values to be compared. When the experimental and simulation results are close in value (<0.1% difference), the dielectric constant and loss tangent associated with the results can be concluded to be the correct values. Since the chip will be working in the 0-10 GHz range initially, it is more important that the average resonant spacing matches below 10 GHz rather than over the whole range as there are other effects at higher frequencies that can affect the data.

First, the loss tangent is kept constant and the dielectric constant is varied until the

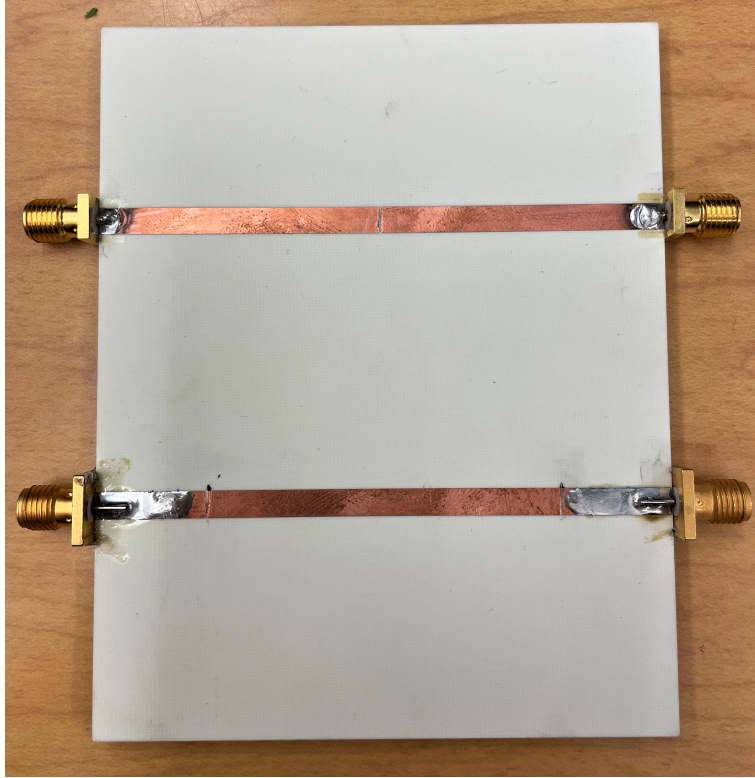


Figure 3.17: Macroscopic Image of Rogers resonators. The one-gap resonator is on the top and the two-gap resonator is on the bottom. Zoomed in images of the gaps are shown in figures 3.18 and 3.19.

average resonance spacing from the simulation is on par with the experimental data. The code used to find the resonances, average resonance spacing, and percent difference between the experiment and simulation is given in Appendix B. Table 3.7 lists the average resonance spacing for the simulation as well as the % difference. The experimental data was found to have an average resonance spacing of $\Delta f = 1.637 \text{ GHz}$, so the % difference is with reference to that value.

The value given for ϵ_r of Rogers RO4350B in the data sheet is 3.66. The plot in which the simulation has this value is given in figure 3.22. However, $\epsilon_r = 3.77$ gave a lower average percentage difference, indicating that this is closer to the true value based on the experiment. This plot is shown in figure 3.23. To determine the error of this method, the dielectric constant with the lowest percent difference was determined for the lowest two resonances (between 0 GHz - 4 GHz) and the highest two resonances (between 8 GHz - 10.5 GHz). The

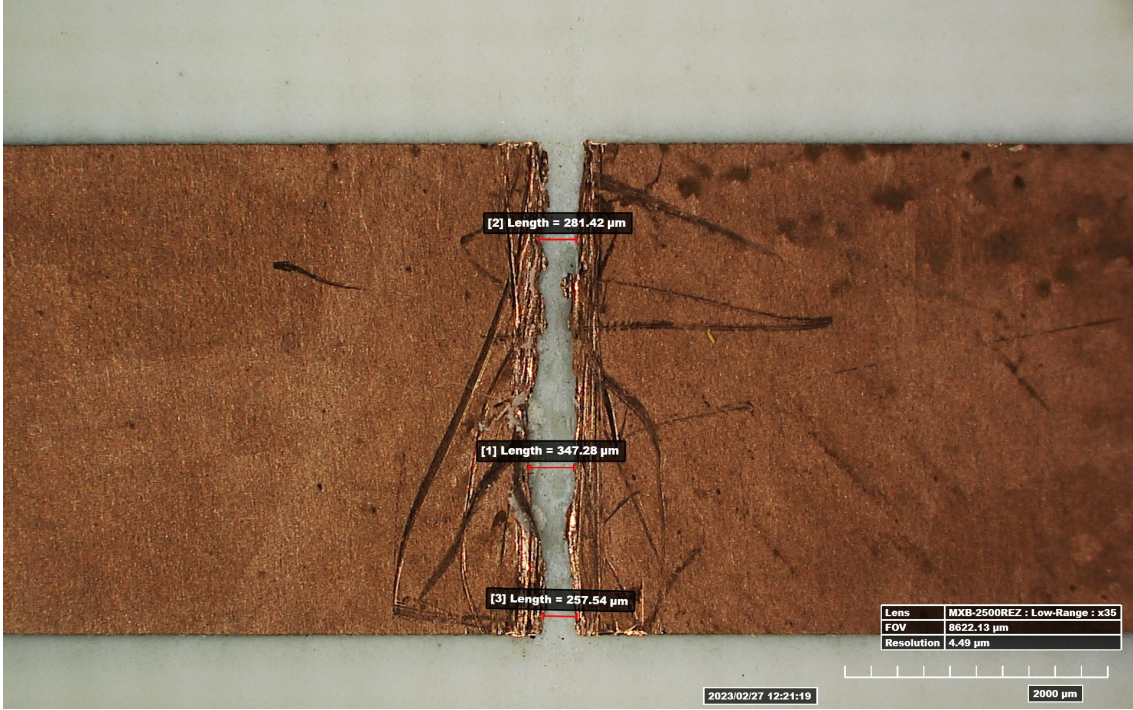


Figure 3.18: x35 magnification and measurement of the gap of the one-gap resonator.

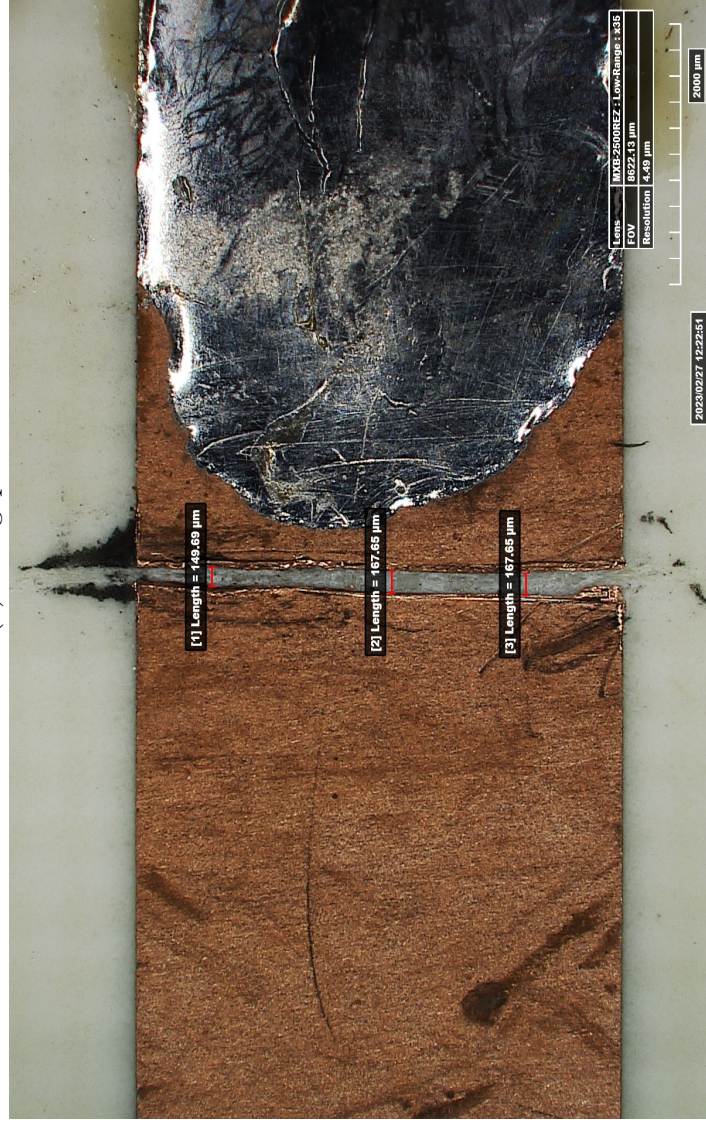
$\epsilon_{r,sim}$	$\Delta f_{avg}(GHz)$	% Difference from Experiment
3.60	1.670	1.99%
3.66	1.653	0.92%
3.70	1.640	0.12%
3.75	1.640	0.12%
3.77	1.637	0.03%
3.81	1.628	0.57%

Table 3.7: Comparison of resonance spacing for 2-gap resonator models with different dielectric constants

lowest two resonances were most similar in terms of resonance spacing to $\epsilon_r = 3.77$ with a percent difference of 0.11% while the highest two were most similar to $\epsilon_r = 3.66$ with a percent difference of 0.31%. From these error bounds, the dielectric constant of the Rogers RO3450B substrate is concluded to be $\epsilon_r = 3.77 \pm 0.11$.



(a) Left gap



(b) Right gap

Figure 3.19: x35 magnification and measurement of the gaps of the two-gap resonator.

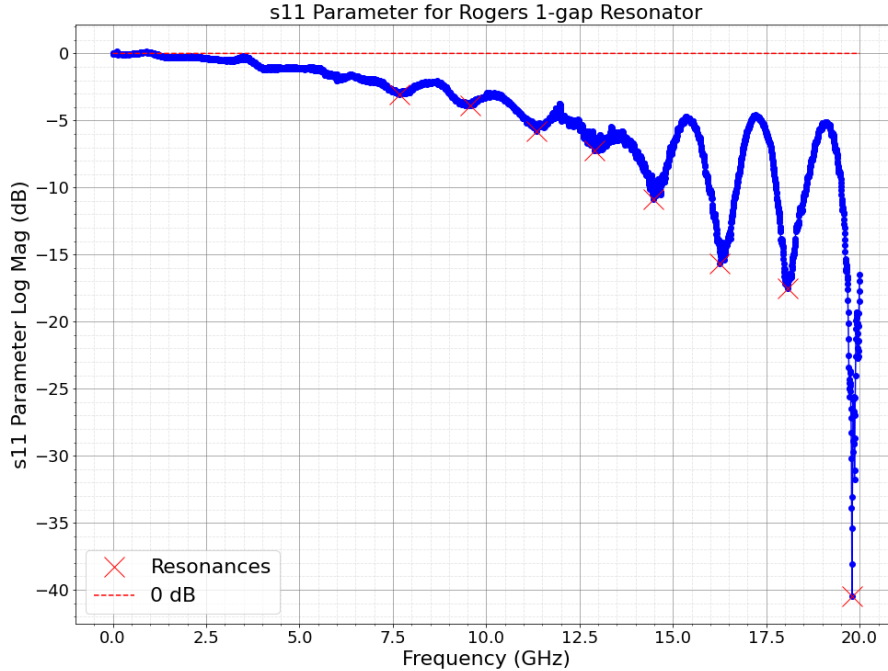


Figure 3.20: Experimental results obtained from the VNA for the reflection coefficient (s_{11}) vs. Frequency for 1-gap Rogers resonator of figure 3.17.

3.2.5 Extracting the Loss Tangent

After determining the dielectric constant to be $\epsilon_r = 3.77 \pm 0.11$, this value for ϵ_r was kept constant while the loss tangent $\tan(\delta)$ was varied to extract it from the experimental data. The loss tangent is related in part to the width of the resonances. To showcase this dependence, a variety of $\tan(\delta)$ values were simulated. These results are shown in figure 3.24.

Though the resonance depth is also related to the loss tangent, several other factors also affect that value, such as the width of the gaps, conductivity of the metal, etc. Therefore, the width of the resonances is a more accurate metric for determining the loss tangent in particular, because it is a frequency measurement. The framework is as follows: convert the data from a logarithmic scale to a linear scale, find the width at half-max of each resonance, and then compare the experimental resonance width to the simulated resonance widths for a range of loss tangents. As the dielectric constant was primarily of interest, this analysis

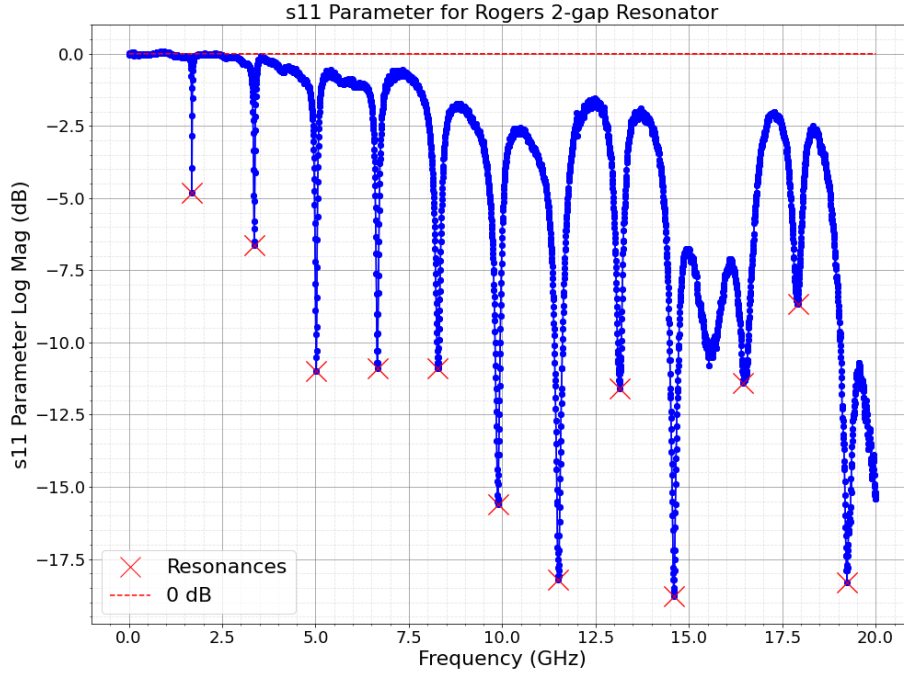


Figure 3.21: Experimental results obtained from the VNA for the reflection coefficient (s_{11}) vs. Frequency for 2-gap Rogers resonator of figure 3.17.

has yet to be completed.

From a qualitative viewpoint, the widths of the resonances from the simulation with $\tan(\delta) = 0.0037$ seem to be quite similar to the experimental values. From figure 3.24 it becomes difficult to distinguish the data from simulations with $\tan(\delta) = 0.001$ or below, indicating that a different measurement technique may be needed for loss tangent values that are smaller than 0.001. Since the widths are already quite similar for $\tan(\delta) = 0.0037$, it is unlikely that the true value is an order of magnitude different (as it would need to be distinguishable), so determining $\tan(\delta)$ may prove to be more difficult than determining the dielectric constant.

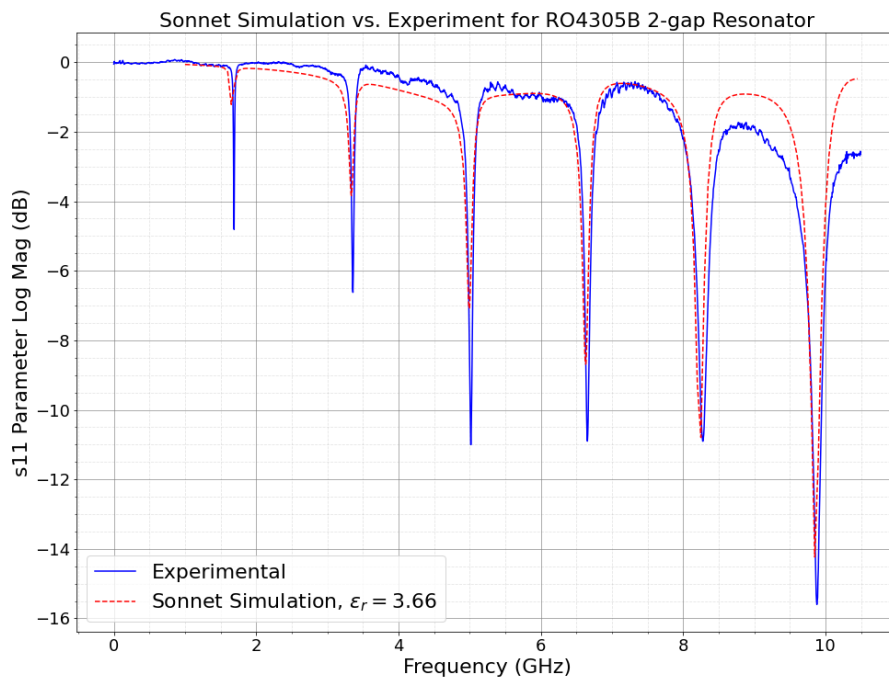


Figure 3.22: Sonnet Simulation of reflection coefficient vs. frequency for 2-gap Rogers resonator with $\epsilon_r = 3.66$ compared to experimental data, from figures 3.7a and 3.17, respectively.

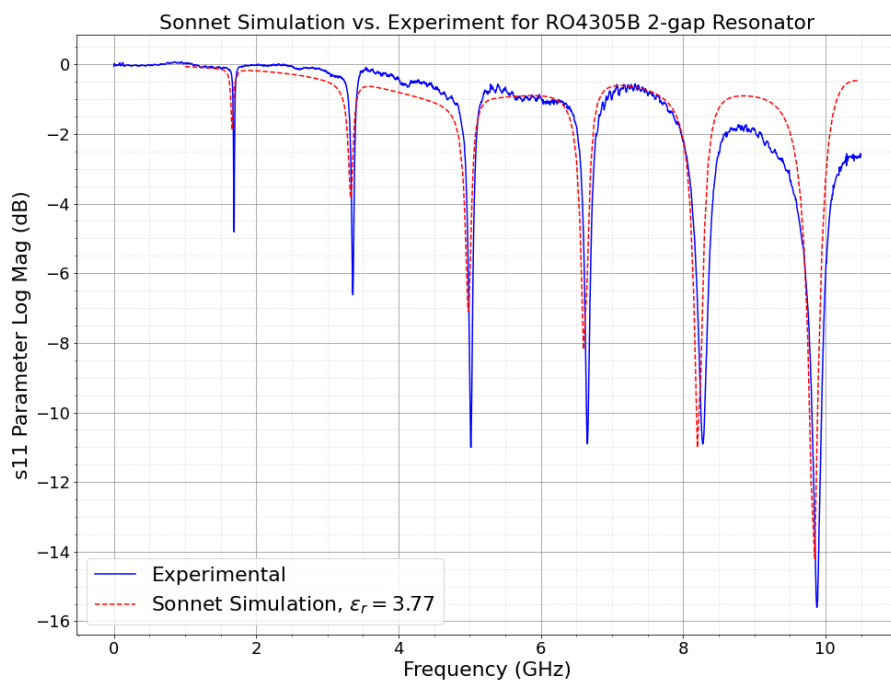


Figure 3.23: Sonnet Simulation of Reflection coefficients vs. Frequency for 2-gap Rogers resonator with $\epsilon_r = 3.77$, from figures 3.7b and 3.17, respectively.

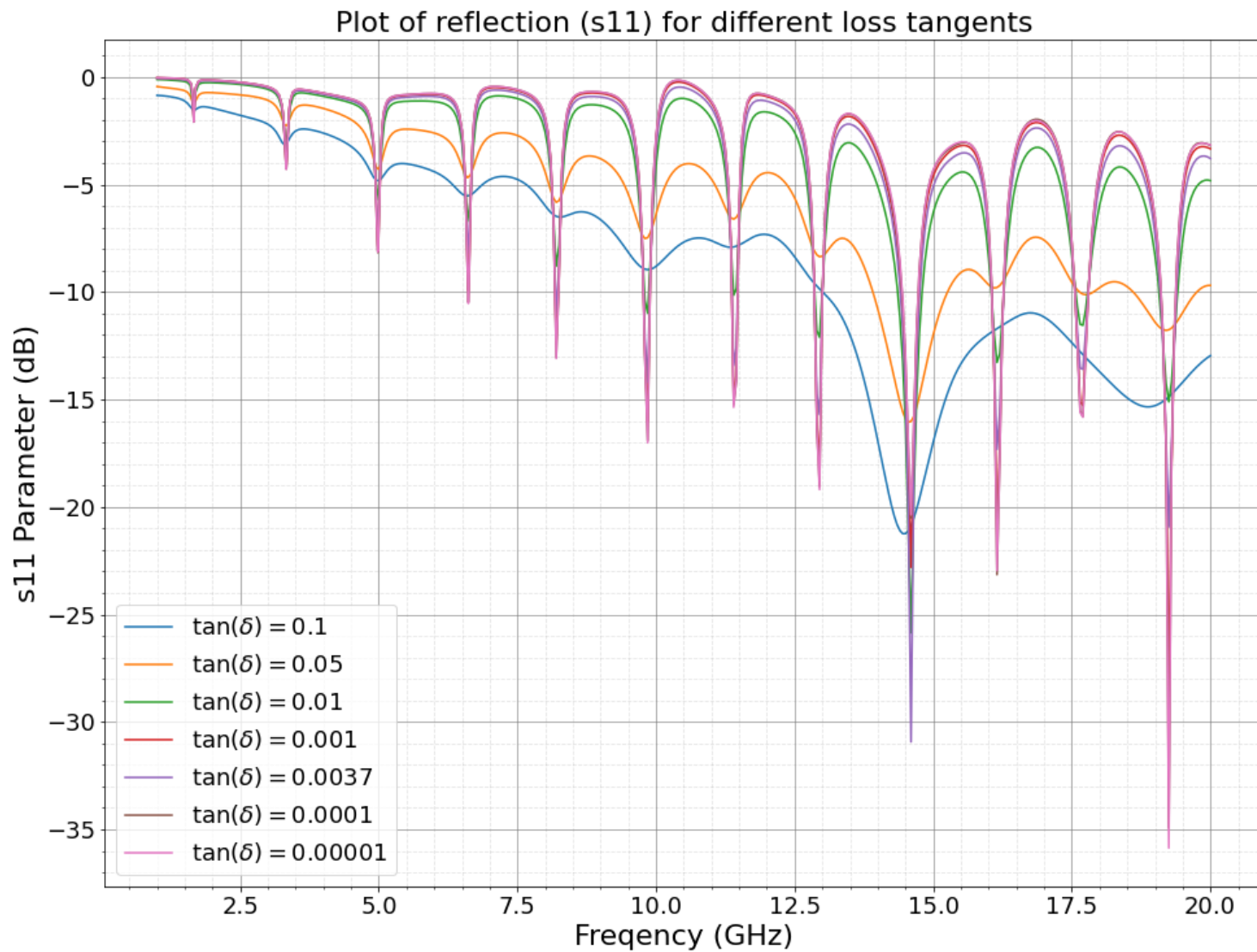


Figure 3.24: Sonnet Simulation of Reflection coefficients vs. Frequency for a variety of loss tangent values. ϵ_r is kept constant at 3.77 for the model of figure 3.7a.

Chapter 4

Power Testing of Current Co-planar Waveguides and Microstrips

4.1 Experimental Setup

Next, the maximum current that the chip will be able to handle was characterized/studied. To do this, an existing co-planar waveguide (CPWs) and a microstrip were used. A CPW is made of a substrate with one metal middle trace and two top metal ground planes made of the same metal. There are also little holes surrounding the ground planes (called vias) to connect the top planes to the bottom ground plane. A microstrip simply consists of a substrate with a small trace of metal in the middle and a bottom ground plane. The CPWs and microstrips in this experiment use AlN as their substrate and copper (thickness of $50\ \mu m$) for the metal traces and ground planes.

The first step is attaching two sets of wires (4 wires in total) to either side of the CPW; this is to be able to do a 4-point measurement, which includes sending a current through one set of wires and measuring the voltage through the other set. Attaching the wires is a challenge in itself, as outlined in section 4.1.1. As shown in figure 4.1, one set of wires is connected to a power supply and an ammeter to provide and measure the current, while the

other set is connected to an oscilloscope to measure how the voltage changes over time. A digital multimeter (DMM) is added to measure the voltage that the setup levels out at and a low-pass filter is added to decrease noise of the signal through the oscilloscope.

After the wires are attached, the CPW/microstrip must be attached to a heat bath because the currents can get relatively high in this experiment. To do this, the CPW is attached to a large copper block, then that copper block is submerged in a bath of water.

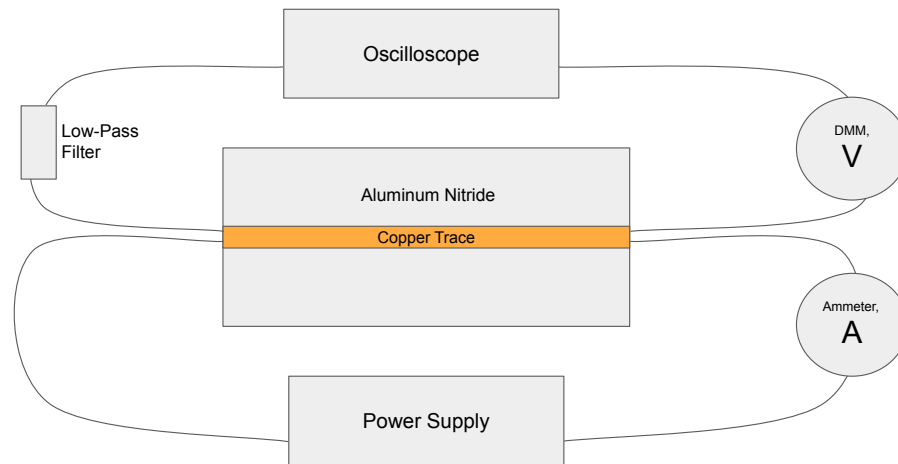


Figure 4.1: Circuit used for power testing experiment with a microstrip

After the setup is complete, a current is sent through the middle trace, and the voltage over time is measured. If the CPW trace can handle this current, it will slowly increase and level out eventually, as shown in figure 4.2a. If the current is too large for the CPW, the voltage will blow up to infinity over time, as shown in figure 4.2b.

4.1.1 Challenges in Adhering Wires to CPWs

The framework for this experiment is complete, but there are challenges in realizing the physical setup. The first challenge is that solder does not adhere well to the copper trace at room temperature due to the high thermal conductivity of AlN. To combat this, the CPW is placed on a hot plate and heated to just under the temperature of the soldering iron

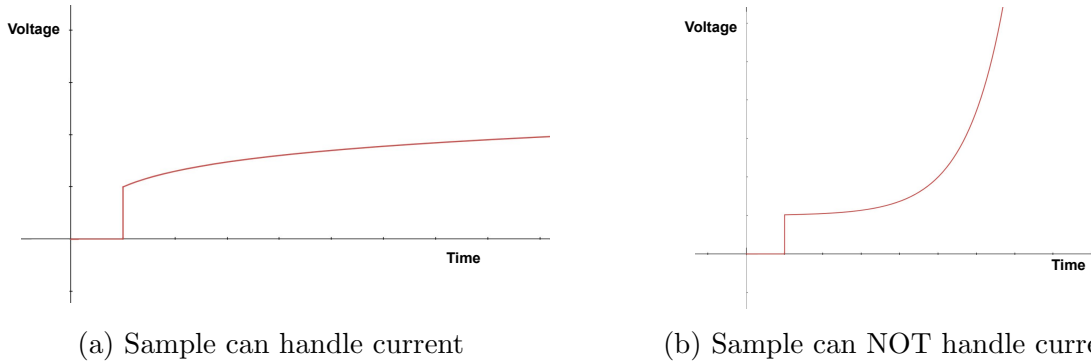


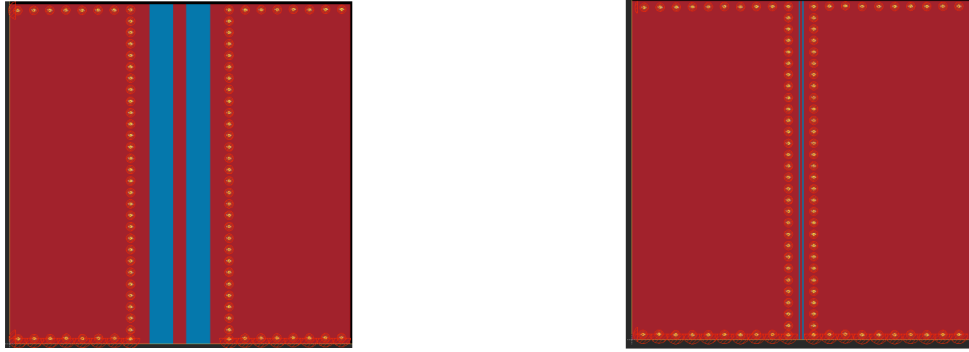
Figure 4.2: Qualitative plots depicting what the voltage plot will look like if the sample (a) can handle the current or (b) cannot handle the current and will break. Before the current source is turned on, the voltage will remain at zero and jump when the source is turned on.

(< 450°C). After it has been heated, the soldering iron is used to give it a final burst of heat to allow the solder to adhere. However, this poses another issue: copper oxidizes incredibly fast at high temperatures, which causes the solder to not adhere well. Therefore, there is a brief window of time in which soldering becomes possible.

This solution worked for the CPW sample with the largest trace of 1 mm and gap width of 2 mm, as shown in figure 4.3a. Because the gap width was large, it was not too difficult to solder the wires directly to the middle trace. However, the other CPWs to be characterized have traces and gaps that are much thinner, such as the one shown in figure 4.3b. This makes soldering significantly more difficult, as there needs to be a good connection between the wires and the center trace without shorting to the outer ground planes with the solder.

A variety of attempts have been made for the CPWs with smaller traces:

- Hand soldering method: The first approach was the same as the one outlines above, with heat-resistant Kapton Tape added to the outer ground planes of the CPWs in order to prevent shorting. However, because the soldering iron is much thicker than the gap between the Kapton tape, it prevented the solder from adhering to the CPW at all.
- Solder paste method: Cover outer ground planes with Kapton tape, put solder paste (SRA Soldering Products SSLTNC-15G was used in this research) onto areas for wires



(a) CPW with a thick trace and gap widths (b) CPW with a thin trace and gap widths

Figure 4.3: CPW Schematics showing differences in trace width and gap width, designed in and adapted from [7]. (a) features gap widths of 2 mm and a trace width of 1 mm, while (b) features gap widths of 0.1 mm and a trace width of 0.2 mm

to connect to trace, place wires, then heat up the entire setup for 5-6 minutes. The solder paste melts and somewhat adheres to the middle trace. This approach has been shown to create an electrical connection to the middle trace without shorting to the outer ground planes, but not a mechanical one as the wires break off from the CPW very easily.

- Conductive epoxy method: This approach is similar to the solder paste approach but has the benefit of not needing to be heated up, as the conductive epoxy used in this research (MG Chemicals 8331D) cures at room temperature. The main issue with this method is that there is not enough room on the middle trace to place enough conductive epoxy to make a good electrical or mechanical connection.
- Conductive and insulating epoxy method: This approach uses insulating epoxy to first make a mechanical connection. The CPW is adhered to a large copper block and the wires are adhered in place using the insulating epoxy. After the wires are mechanically attached, a small amount of conductive epoxy is used to make the electrical connection. Though this kept the mechanical connection, there was still not enough room on the trace to use enough conductive epoxy to create an electrical connection.

The above approaches did not work for adhering wires to the other existing CPWs. Because the outer ground planes do not greatly impact this experiment, the next step would be to chemically etch them off and treat the CPW as a microstrip. Thus the results presented in this thesis in section 4.2 are for the CPW with a thick trace and gap widths as described above and a microstrip with a 0.41 ± 0.01 mm trace.

4.2 Results

For the CPW, currents ranging from 3A to 15A were applied and the voltage change over time was observed. The voltage over time for a 15A current is shown in figure 4.4 (see appendix C for a Python program for converting oscilloscope data to plot). The large jump is when the current source gets turned on, then the current steadily increases until it levels out at around 215.8 mV - this tells us that this CPW can handle a current of at least 15A. To find the maximum current this CPW can handle, a larger current source is needed. However, since the chip will make use of much thinner traces, testing on a microstrip with a 0.41 ± 0.01 mm trace began with the 15A power source.

Like the CPW, currents from 3A to 15A were applied to the microstrip. Figure 4.5 shows the voltage over time for a 15A current. The current was applied for around 70 seconds, then the voltage leveled out around 1.04 V, indicating that this microstrip can handle a current of at least 15A.

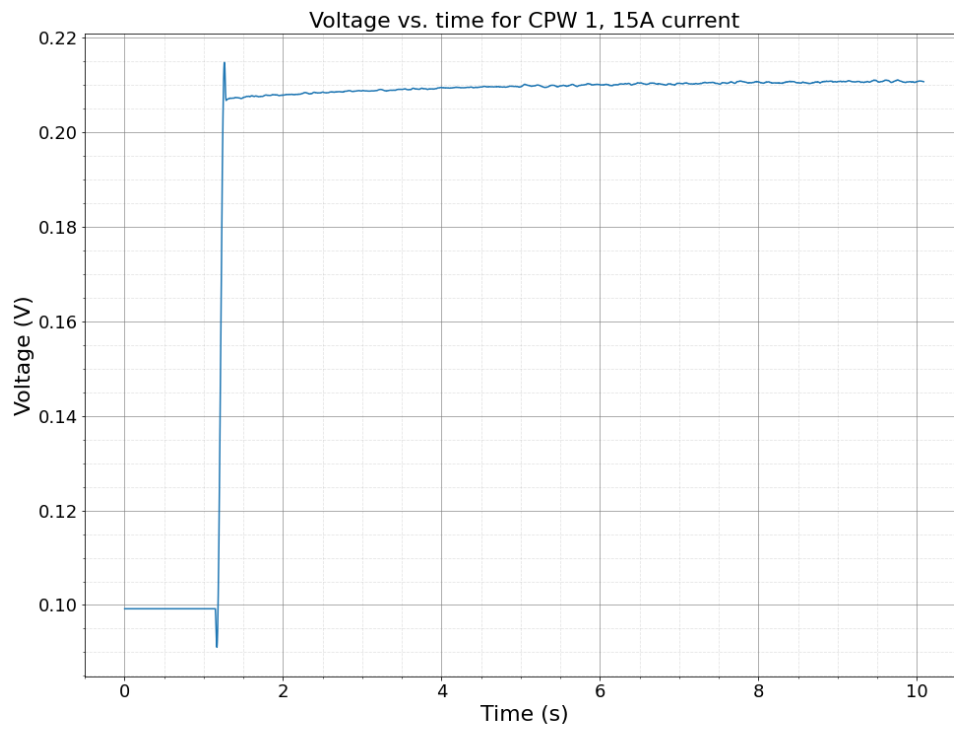


Figure 4.4: Voltage vs. time for 15A current through a CPW with a 1 mm width trace on AlN.

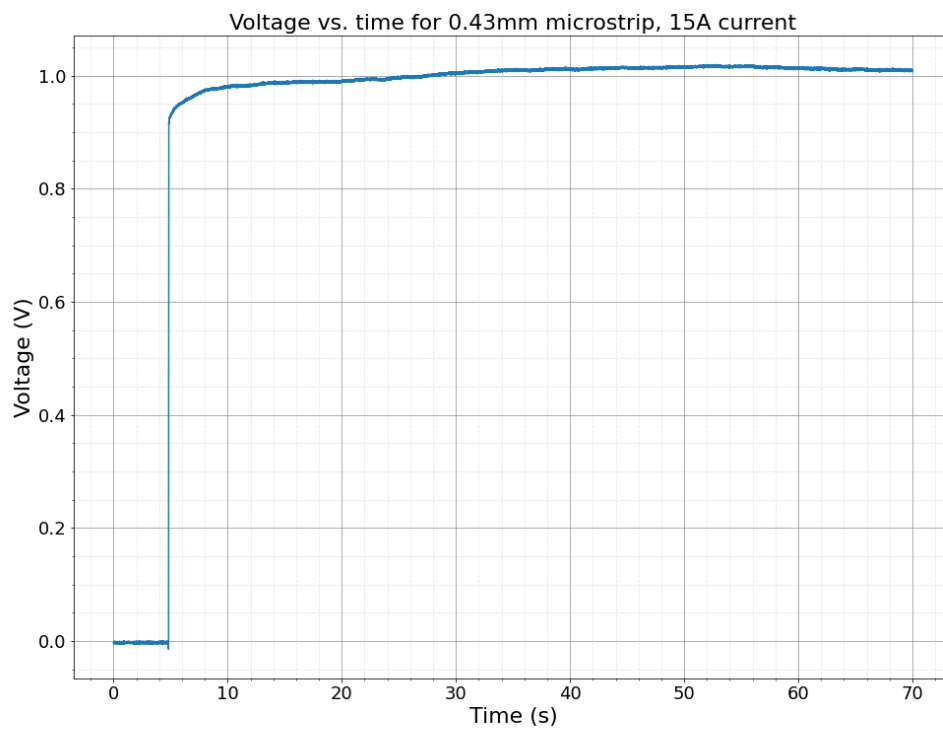


Figure 4.5: Voltage vs. time for a 15A current through a microstrip with a 0.41 mm width trace on AlN.

Chapter 5

Characterizing Quality of AlN and Alumina Samples

To move forward with the project, the lab ordered several rectangular samples of ceramic substrates sandwiched between two copper planes to begin prototyping the chip - these samples will act as a stiff ground plane for the chip to adhere to. They are to be diamond turned to decrease the surface roughness, but characterizing their quality before that process was of interest to the lab. There were 4 sets of samples: (1) a 15 mm x 35 mm sample of AlN sandwiched between two copper planes, (2) a 22 mm x 35 mm sample of AlN sandwiched between two copper planes, (3) a 15 mm x 35 mm sample of alumina sandwiched between two copper planes, and (4) a 22 mm x 35 mm sample of alumina sandwiched between two copper planes. For the remainder of the thesis, the samples will be referred to by their first dimension and composition (e.g. 22 mm Cu-AlN-Cu).

Since the samples were cut from larger rectangles, a random selection of 3 samples from each set of samples was characterized in terms of (1) surface roughness, and (2) dimensions of copper and substrate, and (3) quality of the cuts. The samples were cut by waterjet cutting (Meyer Micro Waterjet, Meyer Tool Huntersville LLC, North Carolina).

5.1 Surface Roughness Measurements

To characterize the surface roughness, a Bruker Dektak XT Surface Profiler was used, which uses a stylus to scan the surface of the sample and automatically calculates the surface roughness (P_a) and root-mean-squared surface roughness (P_q). Table 5.1 gives the surface roughness measurements of the 15 mm Cu-AlN-Cu samples. For sample A, 5 measurements with a scan length of 10 mm were taken. A visualization of these scans is shown in figure 5.1, which shows a slight bowing of the entire sample. To get a more accurate idea of the local surface roughness, two scans with a 3 mm scan length were taken moving forward. An example of the 3 mm scan length taken of the same sample is shown in figure ??, which shows a much more even scan and thus gives more information on the local roughness of the surface itself rather than large scale deformation of the entire substrate.

The measurements of P_a and P_q for 10 mm and 3 mm scan lengths are given for 3 samples for each set in tables 5.1, 5.2, 5.3, and 5.4. To summarize the data, the averages are given in table 5.5. From this, the Cu surfaces of the Cu-Alumina-Cu samples are determined to have significantly higher surface roughness than the Cu-AlN-Cu samples.

P_a Measurements								
Sample	10 mm measurements (\AA)					3 mm measurements (\AA)		
A	7473.89	6873.61	4634.98	4692.88	5111.61			
B	6200.96	8702.94	10536.74			4724.83	6840.06	
C	8012.99	5896.37					5699.62	7710.01
P_q Measurements								
A	9396.69	8801.38	6094.34	7195.32	5948.74			
B	7782.42	10545.67	12263.07			6179.47	9011.09	
C	10616.16	7469.19					8008.18	9595.87

Table 5.1: Measurements of P_a and P_q from the Dektak profilometry of the Cu surface of the 15 mm Cu-AlN-Cu Sample

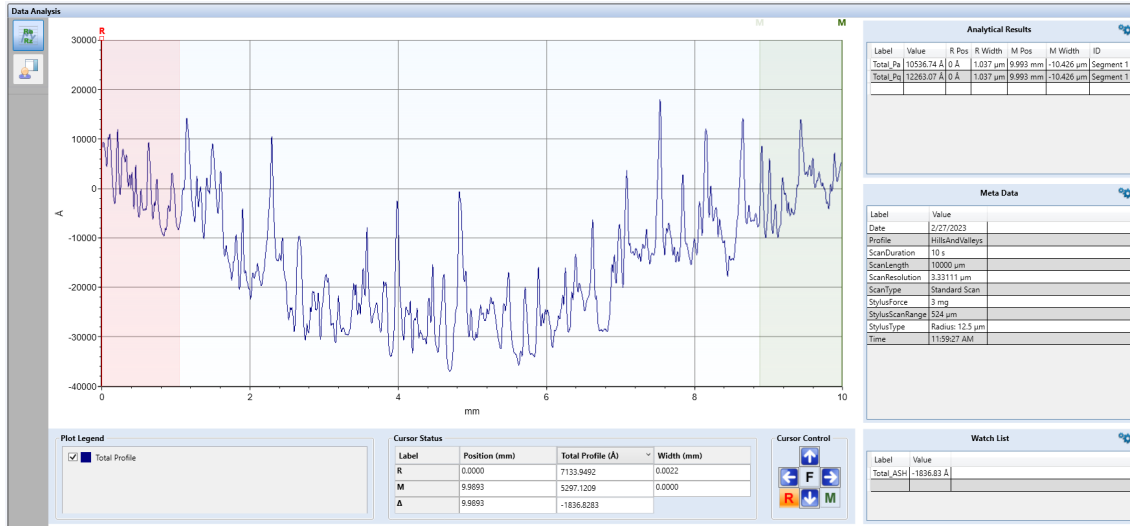
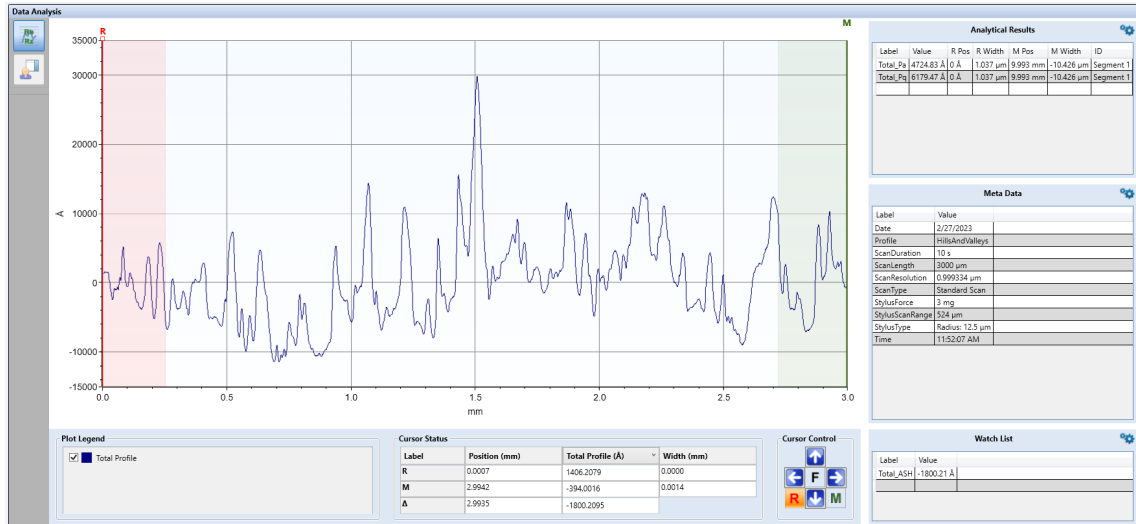


Figure 5.1: Dektak Scan of the Cu surface of 15 mm Al-Cu-Aln with scan length of 10 mm



P_a Measurements					
Sample	10 mm measurements (\AA)			3 mm measurements (\AA)	
A	24146.87	38687.66	238815.59	9390.92	11473.46
B	16760.87	22360.21	14440.2	12506.57	9346.94
C	25252.1	25762.65	34539.00	7830.73	11582.22
P_q Measurements					
A	28205.09	43460.51	29410.81	12127.52	15089.16
B	19528.77	26197.52	17433.68	15975.08	12120.27
C	31584.8	30477.46	39769.49	10229.15	14480.45

Table 5.2: Measurements of P_a and P_q from the Dektak profilometry of the Cu surface of the 15 mm Cu-Alumina-Cu Sample

P_a Measurements					
Sample	10 mm measurements (Å)			3 mm measurements (Å)	
A	11842.71	9362.23	6852.23	4440.08	3815.75
B	13536.72	10899.13	10876.45	4398.09	4502.72
C	6541.35	7214.66	6442.72	5210.57	4464.28
P_q Measurements					
A	14109.99	11001.77	8602.84	5590.23	5021.19
B	16298.38	12835.1	12542.39	5999.31	5598.2
C	7956.25	8626.85	8339.98	6189.66	5929.64

Table 5.3: Measurements of P_a and P_q from the Dektak profilometry of the Cu surface of the 22 mm Cu-AlN-Cu Sample

P_a Measurements					
Sample	10 mm measurements (Å)			3 mm measurements (Å)	
A	54514.87	26892.47	42559.39	10372.53	10166.12
B	45477.27	53603.52	38106.82	7947.79	8645.51
C	46110.05	19409.21	41501.39	12138.11	12004.54
P_q Measurements					
A	62857.31	35433.02	51978.53	12640.4	13389.13
B	51961.11	62323.24	43175.61	10576.09	11411.2
C	55085.13	24925.23	47912.65	15653.09	15222.63

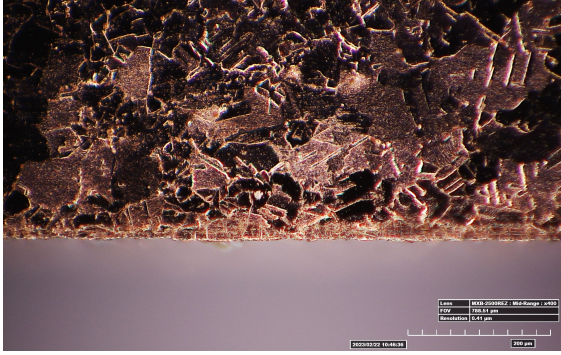
Table 5.4: Measurements of P_a and P_q from the Dektak profilometry of the Cu surface of the 22 mm Cu-Alumina-Cu Sample

Sample	10 mm measurements (Å)		3 mm measurements (Å)	
	Avg. P_a	Avg. P_q	Avg. P_a	Avg. P_q
15 mm Cu-AlN-Cu	6813.70	8611.30	6243.63	8198.65
15 mm Cu-Alumina-Cu	48973.91	29563.13	10355.14	13336.94
22 mm Cu-AlN-Cu	9285.36	11145.95	4471.92	5721.37
22 mm Cu-Alumina-Cu	40908.33	48405.76	10212.43	13148.76

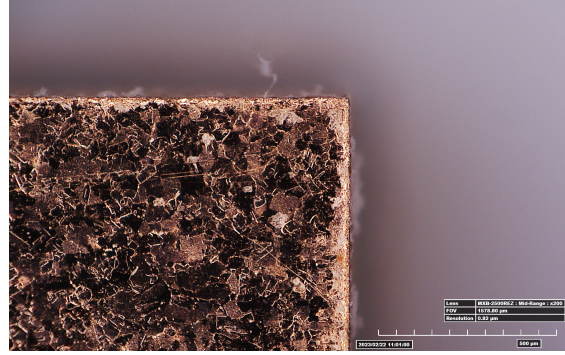
Table 5.5: Average P_a and P_q of all samples, summary of tables 5.1, 5.2, and 5.3, 5.4.

5.2 Characterizing Quality of the Cuts

To measure the dimensions and characterize the quality of the cuts, the samples were looked at under a HIROX RH-2000 Microscope. Because the alumina samples are much rougher as evidenced by table 5.5, the copper planes vary significantly in height in these samples.



(a) Edge of sample A of 15 mm Cu-AlN-Cu



(b) Corner of sample A of 15 mm Cu-AlN-Cu

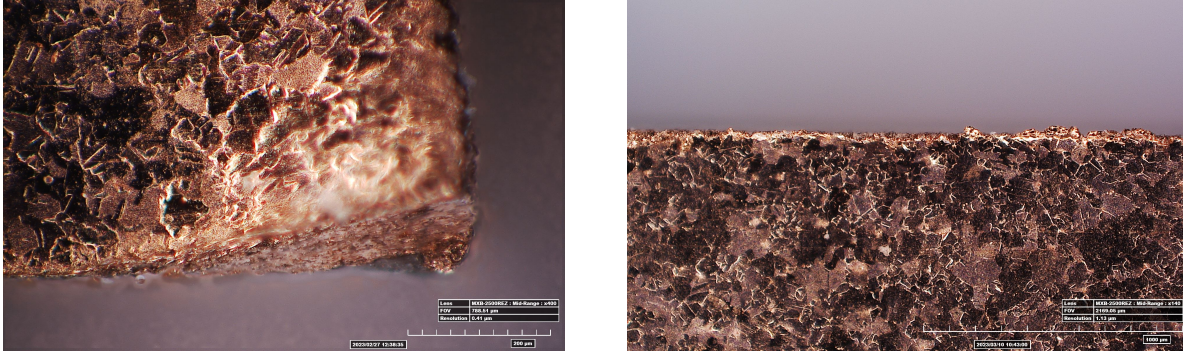
Figure 5.2: HIROX images showing the edge and corner of sample A of 15 mm Cu-AlN-Cu. (a) shows a x400 magnification of the edge of the sample and (b) shows a x200 magnification of the corner.

The AlN samples generally have one copper plane that varies in height while the other is relatively constant. Therefore, the AlN samples have generally higher-quality cross-sections but they generally have lower-quality cuts from a top-down view than the alumina samples. In the following sections, each sample set is discussed in more depth.

5.2.1 15 mm Cu-AlN-Cu Samples

The corners and edges of sample A are very straight and clean, as shown in figure 5.2. Samples B and C, however, show rougher edges and corners, as shown in figure 5.3. Figure 5.3a uses the multi-focus feature of the HIROX, allowing us to see multiple levels of depth, indicating that this corner slopes downward instead of being a clean cut. This is also seen in the other corners of sample B and sample C.

The cross-sections of all 3 samples show relatively high-quality cuts. For each sample, an image was taken of the leftmost edge, middle, and rightmost edge of the cross-section in order to determine whether the copper and substrate planes stay the same height throughout the sample. These images for sample A are shown in figure 5.4. Though the cuts are of high-quality, the height of the uppermost copper plane changes dramatically across the sample. On the left, the height is measured to be $244.02 \mu m$. In the middle and on the right, it



(a) Corner of sample B of 15 mm Cu-AlN-Cu (b) Edge of sample C of 15 mm Cu-AlN-Cu

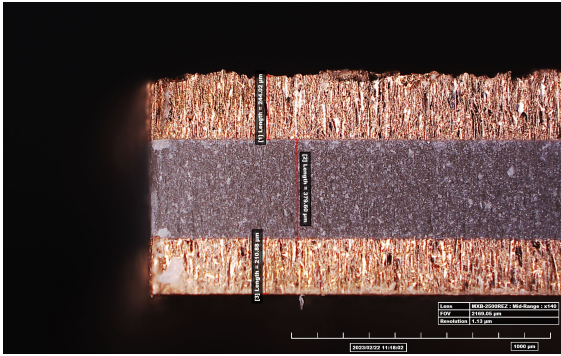
Figure 5.3: HIROX images of 15 mm Cu-AlN-Cu. (a) shows a x200 magnification of the corner of sample B and (b) shows a x200 magnification of the edge of sample C.

is measured to be $265.1 \mu\text{m}$ and $225.99 \mu\text{m}$. This trend can be seen in all of the samples, including the ones with the alumina substrate. This can also be seen from the surface roughness scans from the Dektak: figure 5.1 shows the changing in the magnitude of height. The heights of the AlN substrate and the lower copper plane stay much more constant throughout the sample, only changing by around 5 microns.

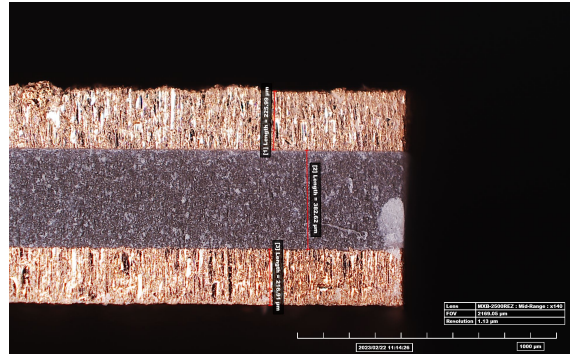
Additionally, a defect was found in the cross-section of sample B. For the most part, the cross-section follows the same trend as sample A excluding the leftmost edge, where the uppermost copper plane can be seen detaching from the AlN, as depicted in figure 5.5.

5.2.2 22 mm Cu-AlN-Cu Samples

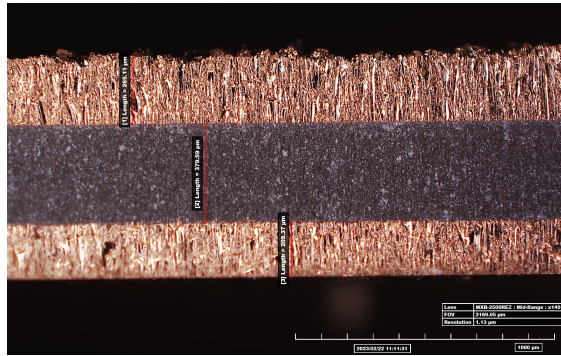
The 22 mm samples of Cu-AlN-Cu followed the same trends as their 15 mm counterparts. The edges of all 3 samples are rough (an example is shown in figure 5.6) while the cross-sections are relatively straight excluding the variance in height of the uppermost copper plane. Sample C had a defect in which the uppermost copper plane took a dip in height at one point near the middle, as shown in figure 5.7.



(a) Left edge of cross-section



(b) Right edge of cross-section



(c) Middle of cross-section

Figure 5.4: HIROX images with x140 magnification of the cross-section of sample A of 15 mm Cu-AlN-Cu. (a) shows the left edge, (b) shows the right edge, and (c) shows the middle of the cross-section.

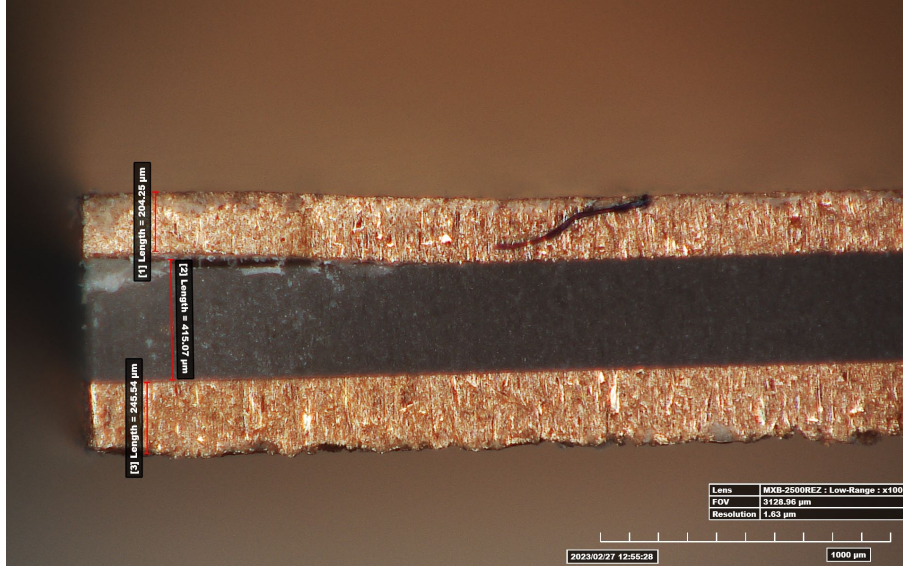


Figure 5.5: HIROX image with x100 magnification showing a defect in the cross-section of sample B of 15 mm Cu-AlN-Cu.

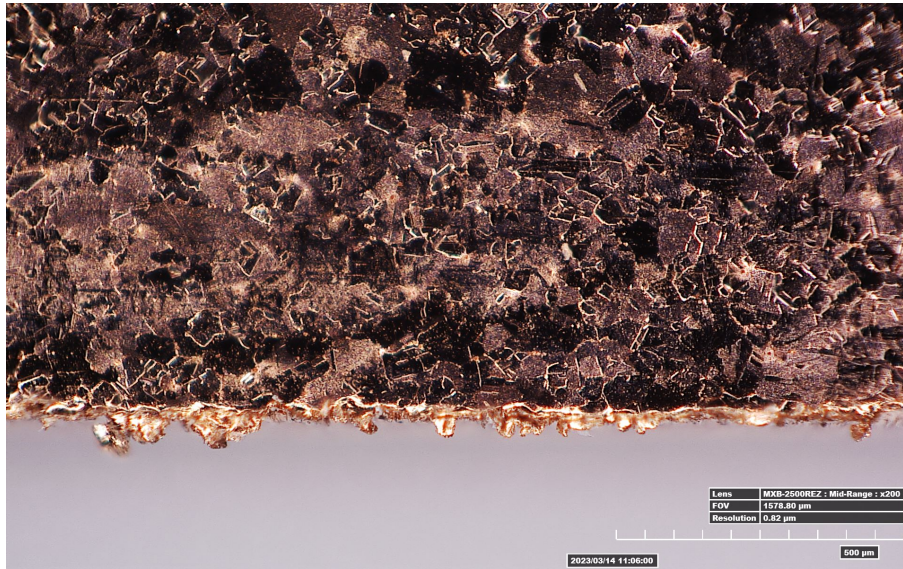


Figure 5.6: HIROX image with x200 magnification showing the edge of sample B of 22 mm Cu-AlN-Cu.

5.2.3 15 mm Cu-Alumina-Cu Samples

The 15 mm Cu-Alumina-Cu samples showed very straight corners and edges compared to the samples with AlN, as shown in figure 5.8. The cross-sections of the alumina samples, however, were of much worse quality than those with AlN. Due to their roughness, the

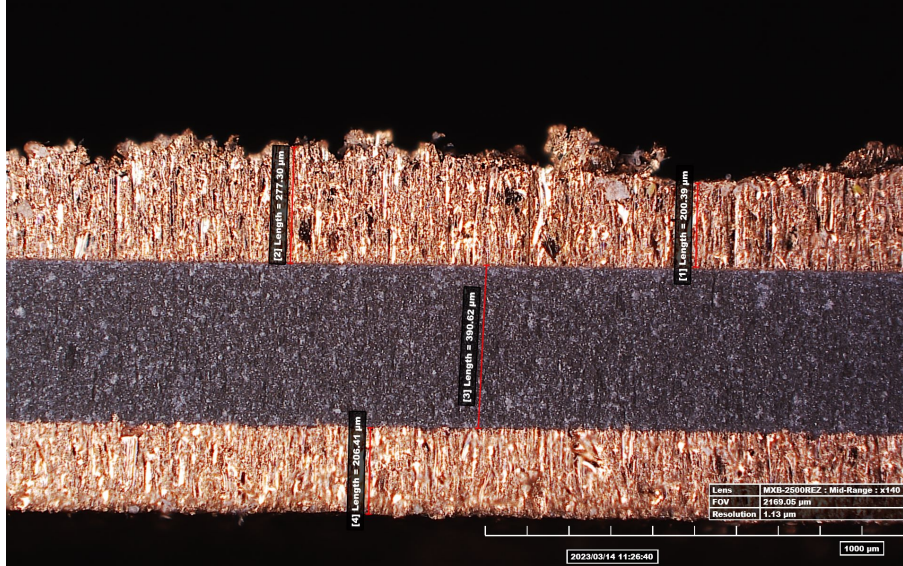
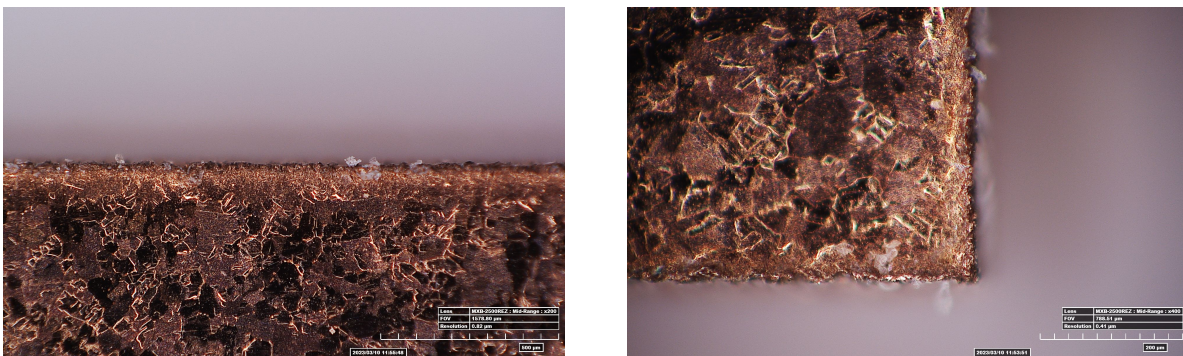


Figure 5.7: HIROX image with x200 magnification showing a defect in the cross-section of 22 mm Cu-AlN-Cu.

heights of the copper planes varied greatly across the samples. Additionally, the alumina substrate is longer than the copper planes, as shown in figure 5.9b.

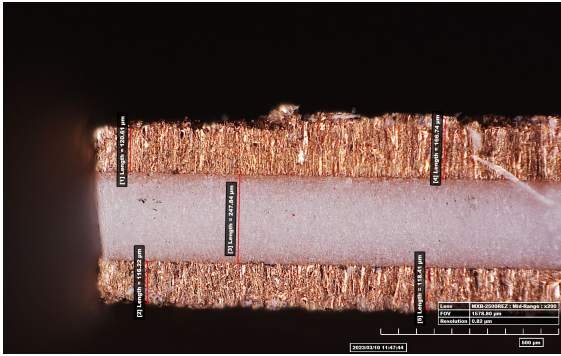
5.2.4 22 mm Cu-Alumina-Cu Samples

Lastly, the 22 mm Cu-Alumina-Cu samples were similar to the 15 mm ones with high quality corners and edges and low-quality cross-sections. Figure 5.10 shows the cross-section of sample A. The blurriness of the leftmost edge is because the edge is not completely straight

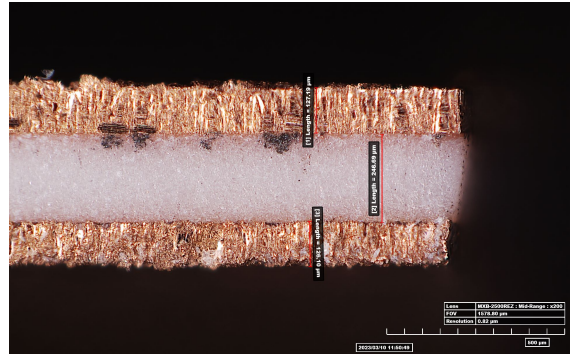


(a) Corner of sample B of 15 mm Cu-Alumina-Cu (b) Edge of sample C of 15 mm Cu-Alumina-Cu

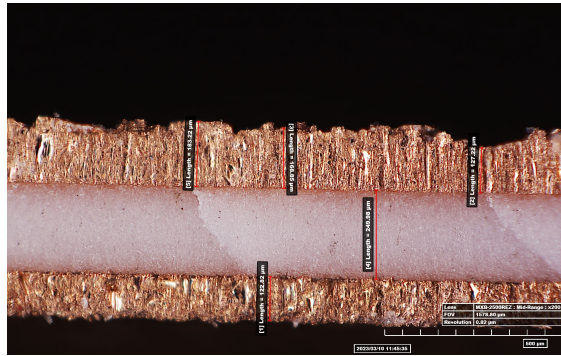
Figure 5.8: HIROX images of 15 mm Cu-Alumina-Cu. (a) shows a x400 magnification of the corner of sample B and (b) shows a x400 magnification of the edge of sample B.



(a) Left edge of cross-section

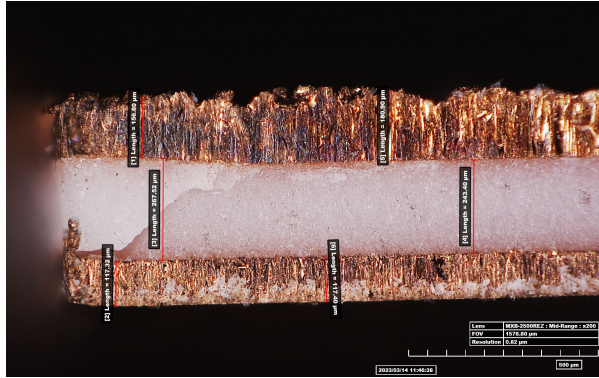


(b) Right edge of cross-section

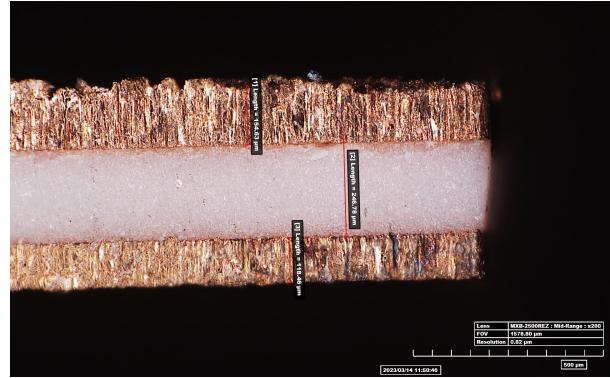


(c) Middle of cross-section

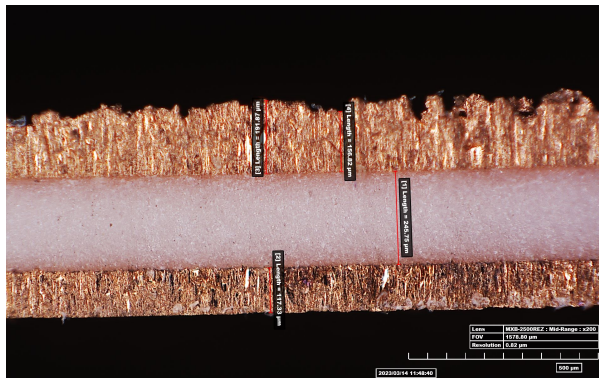
Figure 5.9: HIROX images with x200 magnification of the cross-section of sample A of 15 mm Cu-Alumina-Cu. (a) shows the left edge, (b) shows the right edge, and (c) shows the middle of the cross-section.



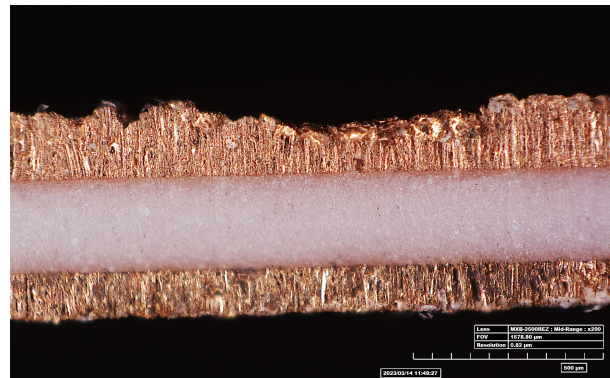
(a) Left edge of cross-section



(b) Right edge of cross-section



(c) Middle of cross-section



(d) Defect of cross-section

Figure 5.10: HIROX images with x200 magnification of the cross-section of sample A of 22 mm Cu-Alumina-Cu. (a) shows the left edge, (b) shows the right edge, (c) shows the middle, and (d) shows a dip in the uppermost copper plane.

down; the HIROX is unable to focus through so many levels of depth. This shows that the cut is not straight in this case. Then, on the right side the alumina substrate can be seen once again coming out of the copper planes as well as a dramatic decrease in the heights of the copper planes. The middle section shows the roughness of the sample. Also included in this figure is a defect of the cross-section in which the copper plane takes a dip in height.

Chapter 6

Conclusion and Future Research

This project successfully characterized and developed a framework for the characterization of properties of materials to be implemented on a microwave atom trap chip. Beginning with attempts to characterize the dielectric constant ϵ_r and loss tangent $\tan(\delta)$, a parallel-plate capacitor approach was first investigated. Several parallel-plate capacitors were created with the aluminum nitride substrate and the Rogers RO4350B substrate from which the capacitance (and thus ϵ_r) and loss tangent could be directly measured with a digital multimeter. Both the dielectric constant and the loss tangent were consistently higher than the accepted values from the datasheet for both materials. For AlN, ϵ_r measurements ranged from 9.6 – 11.7 and $\tan(\delta)$ ranged from 0.004 – 0.03. For RO4350B, ϵ_r measurements ranged from 4.27 – 4.37 and $\tan(\delta)$ ranged from 0.02 – 0.03. The disparities in these values are likely due to the fact that the measurements in this experiment were taken at much lower frequencies than what is reported on the datasheets.

Simulation work on a resonator approach was then started with Sonnet. Though there were some initial roadblocks for this simulation work, the 2-gap resonator design was the most promising. After getting promising results in Sonnet and HFSS, a 1-gap resonator and a 2-gap resonator were fabricated for experimental testing. The 2-gap resonator produced a resonance plot with a number of thin resonances just as the simulations predicted, which

was then used to extract the dielectric constant of RO4350B. This was done by varying the dielectric constant in the simulation until the average resonance spacing below 10 GHz matched up well with the experiment in terms of percent difference. Using this method, the dielectric constant was determined to be $\epsilon_r = 3.77 \pm 0.11$, which is a bit higher than the data sheet reported. The next step for this research is to use the width of the resonances to determine the loss tangent. Using the Rogers substrate provided a proof-of-concept for measuring ϵ_r and $\tan(\delta)$, which can be applied to aluminum nitride after a method of inserting microwaves onto AlN is determined.

Next, the maximum power the chip will be able to handle was characterized using current samples: a co-planar waveguide with a 1 mm copper trace and 2 mm gap width and a microstrip with a 0.41 mm copper trace, both on aluminum nitride. A 4-point measurement was performed to observe the voltage over time for currents ranging from 3A - 15A. Both samples were able to handle a current of 15 A, verifying that an AlN-based chip can work at a fairly high current.

Lastly, samples of aluminum nitride and alumina sandwiched between copper planes were characterized in terms of surface roughness and cut quality. There were 4 sets of samples: (1) a 15 mm x 35 mm sample of aluminum nitride sandwiched between two copper planes, (2) a 22 mm x 35 mm sample of aluminum nitride sandwiched between two copper planes, (3) a 15 mm x 35 mm sample of alumina sandwiched between two copper planes, and (4) a 22 mm x 35 mm sample of alumina sandwiched between two copper planes. The surface roughness of the samples was measured directly by a Bruker Dektak XT Surface Profiler, which gave the general surface roughness P_a and the root-mean-squared surface roughness P_q . It was shown that the samples with alumina are significantly rougher than those with AlN. Next, the quality of the cuts was investigated using a HIROX RH-2000 Microscope. The images and measurements showed that the samples with AlN generally have lower quality cuts than their alumina counterparts, as the edges and corners are rough and slope downward in some cases. The cross-sections of the AlN samples, however, show that the substrate and copper

planes are more consistent in terms of height than the alumina samples, likely due to the differences in surface roughness between the two. The next step for these samples is to get them diamond-turned, a technique used to greatly reduce the surface roughness. They will then be used as the ground plane for the chip.

Overall, this research characterized several properties of materials to be implemented on a microwave atom trap chip. Based on this research, the next step is to further develop the framework for extracting the loss tangent of Rogers RO4350B from resonance plots. This thesis described an approach in which the widths of the resonances could be used; i.e. vary the loss tangent in simulation and compare the width of the simulation vs. experimental data until the percent difference is small, similar to the dielectric constant measurement framework. However, the widths of the resonances (qualitatively) become quite indistinguishable for loss tangents below 0.001, so measuring one resonance at a time may prove to be more useful than averaging all of the resonance widths. The next step is to apply the framework developed for measuring the dielectric constant and loss tangent used for Rogers RO4350B to aluminum nitride. This requires developing a way to effectively insert microwaves onto a chip made from AlN, which the Aubin lab is currently working on. Current efforts include a “wedge” model that tapers the trace from a large size where microwaves can be inserted to a smaller trace that will connect to the microstrip of the chip. Additionally, the power testing experiment could be expanded in two ways: (1) testing more samples, which would require determining a way to effectively attach wires onto current CPW samples, and (2) using currents higher than 15 A to determine the upper limit of current that can be sent through a variety of samples made from AlN. Finally, the big picture goal is to utilize this work and future work that expands upon it in order to design the microwave atom trap chip, fabricate it, and begin testing.

Appendices

Appendix A

Python program for creating plots from Sonnet, HFSS, or VNA data

This is the code used to convert data from Sonnet, HFSS, or the VNA to a plot in Python. By indicating the data type, this one function will be able to plot any of the three.

```
import pandas as pd
import matplotlib.pyplot as plt

def dat_plot(file, dat_type, plt_type, title, saveas):
    '''
    file: input a csv file of raw data from sonnet, hfss, or vna
    dat_type: indicate sonnet ("sim_sonnet"), hfss ("sim_hfss"), or vna ("exp")
    plt_type: color and line for plot (e.g. r--)
    title = title for plot
    saveas = file name to save plot to
    '''

    if dat_type == "sonnet":
        dat = pd.read_csv(file, skiprows = 7)
```

```

    freq = dat["Frequency (GHz)"]
    s11 = dat["DB[S11]"]
    l = "Sonnet"
if dat_type == "hfss":
    dat = pd.read_csv(file)
    freq = dat["Freq [GHz]"]
    s11 = dat["dB(S(1,1)) []"]
    l = "HFSS"
if dat_type == "vna":
    dat = pd.read_csv(file, skiprows=41)
    freq = dat["TR1.FREQ.GHZ"]
    s11 = dat["TR1.LOG MAG.dB"]
    l = "Experimental"

plt.plot(freq, s11, plt_type, label=l)
plt.rcParams["figure.figsize"] = (16, 12)
plt.xlabel("Frequency (GHz)", fontsize = 22)
plt.ylabel("s11 Parameters (dB)", fontsize = 22)
plt.yticks(fontsize=18)
plt.xticks(fontsize=18)
plt.title(title, fontsize=22)
plt.legend(fontsize=22,loc = "lower left")
plt.grid(visible=True,which="major", color = "grey", linestyle="-", alpha=0.8)
plt.grid(visible=True,which="minor", color = "grey", linestyle="--", alpha=0.2)
plt.minorticks_on()

plt.savefig(saveas)

```

Appendix B

Python program for finding resonance spacing and percent difference

This is the code used to find resonances from experimental (VNA) data and simulation (Sonnet or HFSS) data, calculate the average spacing between them, then give the percent difference between the two. The variables [SIM_FILE] and [EXP_FILE] are placeholder variables that the user will input. The program can also find the s11 parameter corresponding to the resonances, helpful for determining the loss tangent.

```
import pandas as pd
from scipy.signal import find_peaks

def res_spacing(file, dat_type):
    '''
    file: input a csv file of raw data from sonnet, hfss, or vna
    dat_type: indicate sonnet ("sim_sonnet"), hfss ("sim_hfss"), or vna ("exp")
    Returns spacing between resonances and s11 parameter at resonances
    '''
    data = pd.read_csv(file)
```

```

if dat_type == "exp":
    f = "TR1.FREQ.GHZ"
    s = "TR1.LOG MAG.dB"
    plot_type="b-"
    d=200

if dat_type == "sim_hfss":
    f = "Freq [GHz]"
    s = "dB(S(1,1)) []"
    plot_type="r--"
    d=1

if dat_type == "sim_sonnet":
    f="Frequency (GHz)"
    s="DB[S11]"
    plot_type="r--"
    d=1

freq = data[f].values
s11 = data[s].values

#find index of 10GHz to remain below
i= 0
for f in freq:
    if f >= 10.5:
        last_ind=i
        break
    i+=1
freq = freq[0:last_ind]
s11= s11[0:last_ind]

```

```

#find resonances
res_ind ,_ = find_peaks(-s11, distance = d) #gives indices of resonances
if dat_type == "exp":
    res_ind = list(res_ind)[1:] #removes false resonance at beginning of exp
    data
resonances = [freq[i] for i in res_ind]
s11_resonances = [s11[i] for i in res_ind]

del_f = [resonances[i+1] - resonances[i] for i in range(len(resonances)-1)]
del_f_ave = (sum(del_f)/len(del_f))

return del_f_ave, s11_resonances

def perc_diff("[EXP_FILE]", "[SIM_FILE]"):
    del_f_exp = res_spacing("[EXP_FILE]", "exp")[0]
    del_f_sim=res_spacing("[SIM_FILE]", "sim")[0]
    perc_diff = ((del_f_sim-del_f_exp)/((del_f_exp+del_f_sim)/2)) * 100
    return perc_diff, del_f_sim, del_f_exp

perc_diff = perc_diff("[EXP_FILE]", "[SIM_FILE]")[0]

```

Appendix C

Python program for plotting power testing data from an oscilloscope

This is the code used to convert .csv data from an oscilloscope to a plot in Python. Notably, the Savitzky-Golay function from the SciPy library [10] is utilized to greatly reduce signal noise and create a smooth plot. The variables [FILE] and [NAME_TO_SAVE_AS] are placeholder variables that the user will input.

```
import pandas as pd
import matplotlib.pyplot as plt
from scipy.signal import savgol_filter

file = "[FILE]"
data = pd.read_csv(file, skiprows=11) #from the scope
df = pd.DataFrame(data)

t = df["Second"].to_list()
t = [i + offset for i in t] #remove offset from scope
volt = df["Value"].to_list()
new_volt = savgol_filter(volt, 101, 3) #smooth data
```

```
plt.plot(t, new_volt, "--")

plt.rcParams["figure.figsize"] = (16, 12)
plt.xlabel("Time (s)", fontsize = 22)
plt.ylabel("Voltage (V)", fontsize = 22)
plt.yticks(fontsize=18)
plt.xticks(fontsize=18)
plt.title("Voltage vs. time for 0.41mm microstrip, 15A current", fontsize=22)
plt.grid(visible=True,which="major", color ="grey", linestyle="--", alpha=0.8)
plt.grid(visible=True,which="minor", color ="grey", linestyle="--", alpha=0.2)
plt.minorticks_on()

plt.savefig("[NAME_TO_SAVE_AS]")
```

Appendix D

Creating gap resonators in Sonnet

There were some difficulties in creating a high-quality gap resonator model so below are some useful tips discovered through this research for refining a resonator model in Sonnet. These changes helped quite a bit for the gap resonators (figures [3.7a](#) and [3.7b](#)), but less so for the stub resonators (figures [3.7c](#) and [3.7d](#)).

1. Increase the thickness of the air layer above the main trace (5 mm was used in this research). A thin layer of air can result in the top box cover coupling to the trace, producing inaccurate results.
2. Set top box cover to Free Space (Settings → Box → Top metal → Free Space)
3. Change port length settings. This tip will include some trial and error, but for this research, a 6 mm fixed port length produced the best results.
4. If the resonator model is symmetric, check Symmetry option in Settings → Box.
5. Check Enhance Resonance Detection in Settings → EM Options → Advanced Options.
6. Reduce the box size when able. For example, the Y dimension can be much smaller than the same as the X dimension, which will reduce simulation run times.

Bibliography

- [1] Griffiths, David. *Introduction to Electrodynamics*. 4th ed., Pearson. **2013**.
- [2] William Miyahira, Andrew P. Rotunno , ShuangLi Du, and Seth Aubin. “Microwave Atom Chip Design”. *Atoms* **2021**, *9*, 54. <https://doi.org/10.3390/atoms9030054>
- [3] Precision Ceramics. “Aluminum Nitride PCAN1000”. **2023**.
<https://precision-ceramics.com/wp-content/uploads/pc-usa-datasheet-aluminum-nitride-pcan1000-2022-03-27.pdf>
- [4] Zhaolin Lu, Janusz A. Murakowski, Christopher A. Schuetz, Shouyuan Shi, Garrett J. Schneider, Jesse P. Samluk, and Dennis W. Prather. “Perfect Lens Makes a Perfect Trap”. *Optics Express* **2006**, *14*, 6.
- [5] S. Aubin and V. Avrutin. “VMEC Seed Proposal on Microwave Tweezer”. **2020**.
- [6] Andrew Beling. “Progress Towards Electromagnetig Manipulation and Trapping of Micro-particles”, undergraduate honors thesis, College of William and Mary. **2021**.
- [7] Morgan Logsdon. “Co-planar waveguides for microwave atom chips”, undergraduate honors thesis, College of William and Mary. **2022**.
- [8] Stephen Rosene. “Progress Toward Microwave Near-Field Manipulation of Micro-Objects”, undergraduate honors thesis, College of William and Mary. **2022**.
- [9] Rogers Corporation. “RO4000 Series High Frequency Circuit Materials”. **2018**.

- [10] SciPy Documentation. “scipy.signal.savgol_filter”. https://docs.scipy.org/doc/scipy/reference/generated/scipy.signal.savgol_filter.html
- [11] Charles T. Fancher. “AC Zeeman Force with Ultracold Atoms”, Ph.D. thesis, College of William and Mary. **2017**.
- [12] Schuangli Du. “AC & DC Zeeman Interferometric Sensing with Ultracold Trapped Atoms on a Chip”, Ph.D. thesis, College of William and Mary. **2021**.